ACS Catalysis

pubs.acs.org/acscatalysis Review

Electrochemical Reduction of CO_2 using Solid Oxide Electrolysis Cells: Insights into Catalysis by Nonstoichiometric Mixed Metal Oxides

Elif Tezel, Ariel Whitten, Genevieve Yarema, Reinhard Denecke,* Jean-Sabin McEwen,* and Eranda Nikolla*

Cite This: *ACS Catal.* 2022, 12, 11456−11471 Read Online

ABSTRACT: Selective electrochemical reduction of CO_2 using renewable energy sources to create platform molecules for synthesis of fuels and chemicals has become a contemporary research area of interest because of its potential for recycling and minimizing the adverse environmental impacts of CO_2. Solid oxide electrolysis cells (SOECs) are solid-state electrochemical devices with significant potential in this area because of their ability to efficiently and selectively convert CO_2 to CO or, when coupled with water electrolysis, to produce syngas (CO and H_2). Both CO and syngas are precursors for the synthesis of fuels and chemicals using existing technologies. While promising, SOECs are limited by the instability of the state-of-the-art cathode electrocatalyst, Ni/yttria-stabilized zirconia (YSZ) cermet, due to its limited redox properties and deactivation by carbon deposits. Nonstoichiometric mixed ionic and electronic conducting oxides are promising alternatives because of their redox stability and resistance to deactivation by carbon. Herein, we summarize the literature in this area and derive trends that relate changes in composition and oxygen defects in these oxides to activity, selectivity, and stability for the electrochemical reduction of CO_2 to CO in SOECs using both experimental and theoretical studies. We also evaluate the factors that present challenges in a direct comparison of the performance of SOEC cathode electrocatalysts for CO_2 reduction reported in the literature and suggest possible solutions and standardized protocols for benchmarking the performance of SOECs. We conclude by summarizing and providing an overview of challenges in the field along with potential solutions and opportunities for electrochemical reduction of CO_2 by nonstoichiometric mixed metal oxides in SOECs.

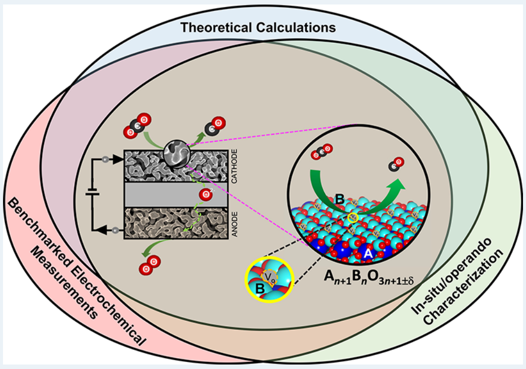

KEYWORDS: *electrochemical CO_2 reduction, nonstoichiometric mixed-metal oxides, solid oxide electrolysis cells, CO_2 recycling, perovskites, X-ray photoelectron spectroscopy, density functional theory, field-assisted catalysis*

1. INTRODUCTION

Global energy demand has been continuously increasing due to steady growth in the worldwide population and industrialization. Currently, the dominant sources of energy supply involve combustion of fossil fuels, which are rapidly depleting and cause adverse environmental effects via generation of greenhouse gases, such as CO_2. A solution to this challenge is to eliminate the use of fossil fuels as the source of energy and commodity chemical production; however, this will require significant developments in renewable energy technologies and changes in infrastructure. An approach to alleviate the detrimental effects of atmospheric CO_2 from existing industrial processes is to utilize renewable energy resources (i.e., solar and wind energy) to power processes that convert CO_2 into platform chemicals, which can be subsequently converted to a wide array of commodity chemicals and fuels using existing technologies such as Fischer−Tropsch synthesis.[1] Significant evolution in CO_2 capture and utilization processes has occurred over the past decade for the generation of value-added carbon-containing chemicals and fuels from atmospheric CO_2.[2−6]

CO_2 is characterized by strong C−O bonds, making this compound very stable and inert, requiring a significant amount of energy for its activation.[7] Processes to convert CO_2 into high-value products have been multifaceted, including thermal catalysis, and photo- and electro-catalysis.[8−14] Among these, electrocatalytic processes have shown promise, since product

Received: July 14, 2022
Revised: August 29, 2022

https://doi.org/10.1021/acscatal.2c03398
ACS Catal. 2022, 12, 11456−11471

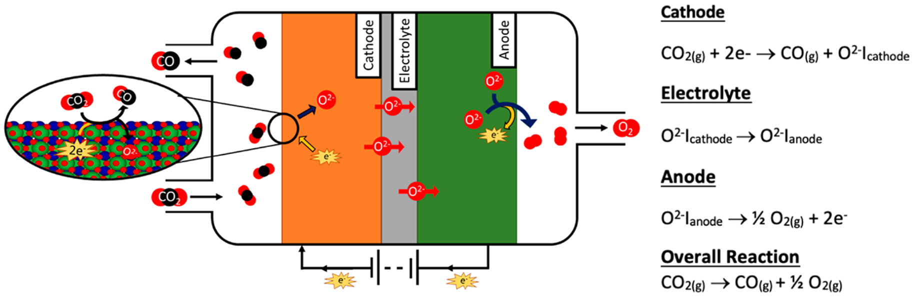

Figure 1. Schematic of electrochemical CO_2 reduction to CO in a SOEC along with the half-cell reactions at each electrode and the overall reaction. The enlarged image highlights the half-cell reaction at the SOEC cathode involving the reduction of CO_2(g) to CO(g) and O^{2-} ions in the presence of electrons.

selectivities and yields from CO_2 can be tuned through adjusting the applied potential under mild reaction conditions, while circumventing the complexity of photocatalytic systems associated with direct coupling of photon and electron processes. Different types of electrochemical systems have been investigated for CO_2 electroreduction over the years.[12,15,16] This review mainly focuses on high-temperature electrochemical reduction using solid oxide electrolysis cells (SOECs) for converting CO_2 selectively to CO. CO is a valuable platform chemical with a wide range of industrial applications: for example, the synthesis of acetic acid by catalytic carbonylation of methanol and the production of formic acid by hydrolysis of methyl formate.[17−19] CO can also be coupled with H_2 and converted to liquid hydrocarbons using Fischer−Tropsch synthesis.[20,21] The electrochemistry at the solid/gas interface of the SOEC cathode is generally simpler than that of low-temperature electrochemical systems at solid/liquid interfaces.[15] This results in SOECs exhibiting higher energy efficiency, stability, and product selectivity, providing advantages for practical application over current low-temperature electrochemical processes.[22,23]

SOECs are solid-state electrochemical devices that operate at elevated temperatures (>700 °C).[24,25] In SOECs, gaseous CO_2 diffuses to the cathode and is reduced in the presence of electrons to gaseous CO, generating O^{2-} ions in the process (Figure 1). O^{2-} ions are conducted through the electrolyte to the anode, where they are evolved as gas-phase O_2. Yttria-stabilized zirconia (YSZ) is the commonly used electrolyte for SOECs, due to its excellent redox stability, high mechanical strength, low cost, and adequate oxygen ionic conductivity at temperatures >700 °C, which typically limits SOEC operation to this temperature regime. Alternatives have been proposed to lower the SOEC operating temperatures, such as Sc_2O_3-stabilized ZrO_2 (SSZ), Sr- and Mg-doped $LaGaO_3$ ($La_{1-x}Sr_xGa_{1-y}Mg_yO_3$, LSGM), which exhibit much higher ionic conductivities between 400 and 800 °C as compared to YSZ. However, these oxides present different challenges related to their instability and cost.[26,27] Buffer/protecting layers have been added between the electrode and these electrolytes to minimize their instability.[28−30]

Metallic Ni/YSZ cermet is the most commonly used cathode for the reduction of CO_2 in SOECs.[25,31,32] CO_2 activation on this cathode requires an engineered triple-phase-boundary (TPB) interface among Ni, YSZ, and the gas-phase species.[33] The Ni/YSZ interface assists in CO_2 adsorption and activation, facilitating electron conduction,[34] while YSZ conducts oxygen ions.[34] Common challenges with Ni-based cathodes include degradation caused by the oxidation of Ni, particle agglomeration, and carbon deposition.[35−37]

Nonstoichiometric mixed ionic and electronic conducting oxides ($A_{n+1}B_nO_{3n+1\pm\delta}$; $n = 1 \rightarrow \infty$, where $n = 1$ results in a Ruddlesden−Popper phase, while $n = \infty$ results in a simple perovskite phase; A represents rare-earth and/or alkaline-earth-metal cations, while B represents transition-metal cations) have been considered as alternatives to the Ni/YSZ cermet because of their redox stability. In this case, the oxide acts as both the catalytically active surface and the medium for the conduction of electrons and oxygen ions, reducing the TPB to a double-phase boundary interface. These oxides are characterized by coupled ionic and electronic conductivity facilitated by the oxygen nonstoichiometry (δ) in their structure.[38−40] Their main limitation has been the inferior catalytic reactivity as compared to Ni/YSZ. This limitation can be potentially addressed by tapping into the large compositional space of these oxides, which has been fairly underinvestigated in the literature. For example, it has been demonstrated that perovskite oxide structures with 4*d* or 5*d* transition-metal cations diluted among 3*d* transition-metal cations in the B-site can exhibit significantly higher electrochemical rates for oxygen reduction reaction (ORR) in alkaline media in comparison to the supported 4*d* or 5*d* transition-metal counterparts.[41]

In this review, we summarize the current advances in electrochemical reduction of CO_2 by nonstoichiometric mixed ionic and electronic conducting oxides in SOECs. We briefly introduce the fundamentals (thermodynamics and kinetics) of this process, followed by the development of correlations between the oxide composition and oxygen nonstoichiometry with the performance for electrochemical CO_2 reduction from reported experimental and theoretical studies. Based on the challenges with direct comparison of the performances reported across various literature sources, we suggest possible solutions and standardized protocols for benchmarking the performance of SOECs. We conclude by summarizing and providing a perspective on the advancements that are required to make these systems feasible.

2. FUNDAMENTALS OF CO_2 REDUCTION IN SOECS

Electrochemical reduction of CO_2 in SOECs occurs at the cathode in the presence of electrons, forming a mixture of O^{2-} ions and $CO_{(g)}$. The O^{2-} ions are driven by the difference in potential from the cathode to the anode, where they are oxidized and evolved as O_2 in the gas phase. These processes are illustrated in Figure 1. The total energy demand for reduction of CO_2 to CO is described by the change in the Gibbs free energy (ΔG_T) of the overall reaction (CO_2(g) →

$CO(g) + 1/2O_{2(g)}$) evaluated at the reaction temperature. ΔG_T includes effects from changes in enthalpic (ΔH) and entropic (ΔS) energy contributions at the operating temperatures (eq 1). These energetic contributions are plotted in Figure 2 as a function of temperature. ΔH and ΔS values were calculated using the open source NIST Webbook data.[42] Figure 2 shows that increasing the operating temperature leads to a significant decrease in the total energy demand, while the total enthalpic energy demand remains almost constant. This suggests that, with an increase in temperature, the efficiency for CO production increases, arising from entropic effects.[24]

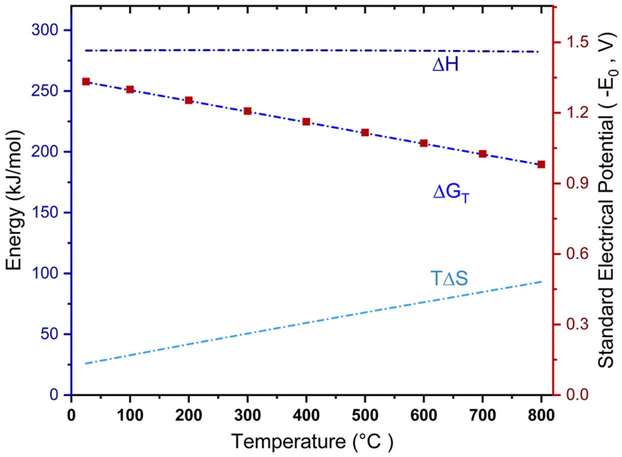

Figure 2. Thermodynamics of electrochemical reduction of CO_2 to CO at atmospheric pressure. ΔH, ΔG_T, and ΔS values were calculated using the data from the NIST Webbook.[42]

$$\Delta G_T = \Delta H - T\cdot\Delta S \tag{1}$$

The required electrical potential (voltage), E_T, at any pressure and temperature can be expressed by the Nernst equation (eq 2). The first term in this equation is the standard electrical potential (E_0) at unit activity and standard pressure, which is related to the Gibbs free energy at the reaction temperature for CO_2 electrolysis, as shown by eq 3. Standard electrical potentials at various temperatures are presented with red square marks in Figure 2, for the secondary y axis.

$$E_T = E_0 + \frac{RT}{2F}\ln\frac{(P_{CO}/P^0)(P_{O_2}/P^0)^{1/2}}{P_{CO_2}/P^0} \tag{2}$$

$$E_0 = \frac{\Delta G_T}{nF} \tag{3}$$

In these equations, F represents the Faraday constant, n represents the number of electrons transferred during the reaction, which is 2 for the reduction of CO_2 to CO, and R represents the gas constant. P_{CO}, P_{O_2}, and P_{CO_2} refer to the partial pressures of CO, O_2, and CO_2, respectively, which are normalized by the standard pressure, P^0. The standard Gibbs free energy change (ΔG^0) at standard operating conditions (25 °C and 1 atm) for CO_2 electrolysis is 257.3 kJ/mol, consistent with the reduction reaction being nonspontaneous under the standard conditions. The corresponding voltage (E_0) under the standard conditions is −1.33 V, which refers to the electrical energy demand required to drive the reduction reaction.

The value of E_T is considered to be equal to the theoretical open-circuit potential (V_{OCV}) of the cell at thermodynamic equilibrium. Once the reaction is driven in the forward direction and the exchange of charge species occurs between the two electrodes, the measured potential V_{Exp} deviates from the thermodynamic potential, V_{OCV}, due to overpotential losses (η_{cell}) in an SOEC (eq 4). The overall η_{cell} has contributions from ionic and electronic resistances (Ohmic overpotentials, η_{Ohmic}), mass transport resistances (concentration overpotential, η_{con}), and the resistances related to the electrode reaction kinetics (activation overpotential, η_{act}).

$$V_{Exp} = V_{OCV} - \eta_{Ohmic} - \eta_{con} - \eta_{act} \tag{4}$$

The overall η_{cell} is dominated by the activation overpotential associated with the kinetics of the half-cell reactions of CO_2 reduction at a low applied potential. As the applied potential increases and kinetic rates become faster, the Ohmic and concentration overpotentials dominate.

The electrochemical half-cell reactions at the cathode (CO_2 reduction reaction) and the anode (oxygen evolution reaction) of SOECs consist of a series of elementary steps, the energetics of which are dictated by the electrocatalysts used (nature of the active sites) in these electrodes. It is generally agreed that the rate-limiting step for CO_2 electrolysis in SOECs is the CO_2 reduction reaction at the cathode, and the limiting steps in this process for most reported catalysts have been associated with the adsorption and dissociation of CO_2 on the catalyst surface.[43,44] CO_2 adsorption energetics on the catalyst surface have been tuned by controlling the oxophilicity of the metal catalysts or the content of alkaline or alkaline-earth elements in the oxide structures.[45−47] A balance in the binding strength of CO_2 on the catalyst surface is required to minimize the accumulation of stable carbonates, which can poison the active sites.[47] The energetics of CO_2 dissociation have also been controlled through tuning the nature of the catalytic site at the cathode. For metal electrocatalysts, it has been shown that the oxophilicity of the metal can be used to predict the kinetic barrier for CO_2 activation.[45,46] We discuss the kinetics of CO_2 reduction on mixed metal oxide electrocatalysts in more detail in Section 4.

3. CO_2 REDUCTION ON NONSTOICHIOMETRIC MIXED IONIC AND ELECTRONIC CONDUCTING OXIDE ELECTROCATALYSTS: EXPERIMENTAL STRUCTURE−PERFORMANCE TRENDS

Various crystal structures and compositions of $A_{n+1}B_nO_{3n+1\pm\delta}$ oxides have been studied as SOEC cathode electrocatalysts for CO_2 reduction. Generally, A-site cations in these oxides have a stabilizing structural effect and are not typically reported to be active for CO_2 reduction.[43,44,48,49] A-site compositions with cations of different atomic size and oxidation state have shown to affect the activity due to effects on the bond strength between B-site cations and oxygen ions in the surface layer and the concentration of surface oxygen defects.[50] Both the B-site cations and surface oxygen vacancies have been linked to CO_2 activation on the surface of these oxides. Below, we discuss in detail the effects of oxide composition on the electrochemical CO_2 reduction activity and CO Faradaic efficiency (selectivity).

3.1. Perovskite Oxides.

Simple perovskites (ABO_3) are the most commonly investigated nonstoichiometric mixed ionic and electronic conducting oxides for electrochemical CO_2 reduction.[28,30,51−75] It is well established that the B-site transition-metal cations in these oxides are responsible for the

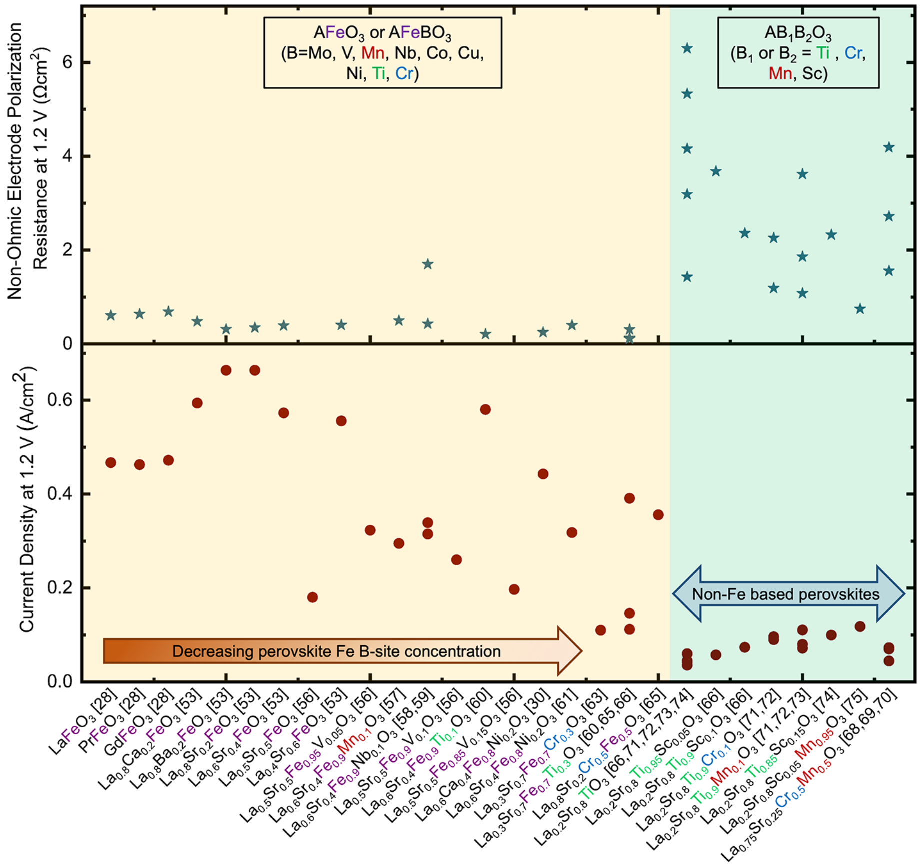

Figure 3. Current densities (absolute values, bottom plot) and non-Ohmic electrode polarization resistances (top plot) of SOECs with cathode perovskite electrocatalysts with Fe in the B-site (yellow region) and those without Fe in their structure (green region) at an applied voltage of 1.2 V and 800 °C.

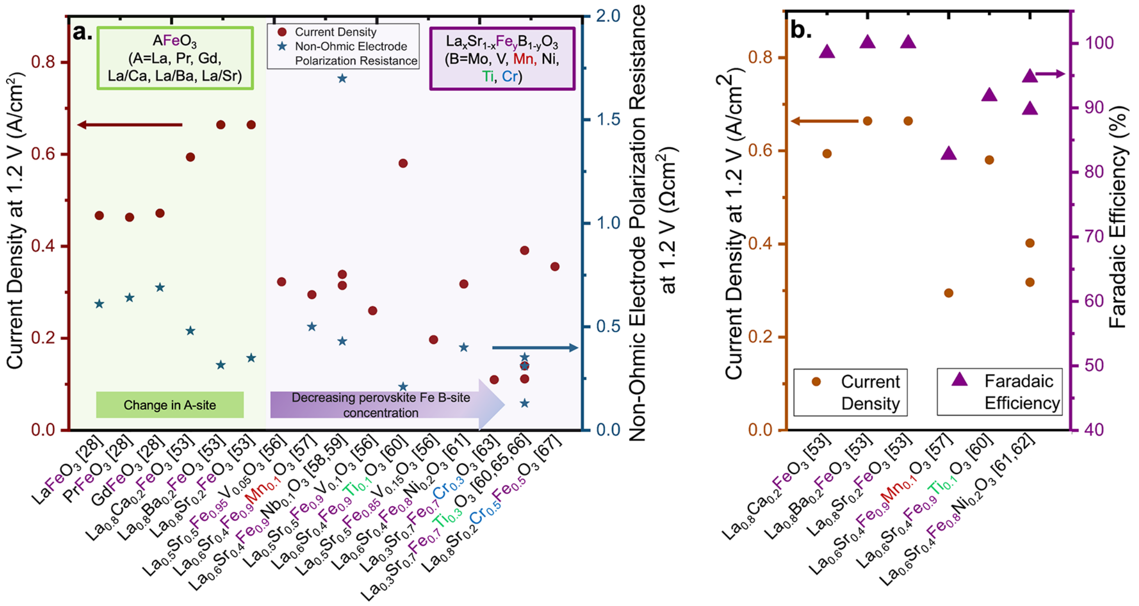

Figure 4. (a) Current densities (absolute values, primary *y* axis) and non-Ohmic electrode polarization resistances (secondary *y* axis) at 1.2 V and 800 °C of SOECs containing Fe-based perovskite cathodes with different A-site compositions (green region) and B-site dopants (purple region). (b) Current densities and CO Faradaic efficiencies (secondary axis) of SOECs containing Fe-based perovskite cathodes at an applied voltage of 1.2 V and 800 °C.

catalytic activity and electron transfer.[76−78] B-site cations are highly hybridized with the surrounding oxygen anions in BO_6 octahedra.[79] Due to B-site hybridization with lattice oxygen, oxygen vacancies interact with the B-site to promote the adsorption and activation of CO_2 on the surface. To determine the effect of the nature of the B-site cations on the CO_2

reduction activity of the ABO_3 oxides, we have plotted the reported absolute values of the current densities and non-Ohmic electrode polarization resistances for electrochemical reduction of CO_2 at 1.2 V and 800 °C for SOECs containing perovskite-based cathodes with varying A- and B-site cation compositions, extracted from the current−voltage (I−V) profiles and impedance spectra of each study, respectively (Figure 3). We focus on the current densities and non-Ohmic resistances at the low-applied-potential region because these are largely dominated by the activation overpotentials associated with CO_2 reduction.

The most commonly reported perovskites for CO_2 reduction are composed of La, Pr, Gd, La/Ca, La/Ba, and La/Sr as A-site cations and Fe, Ti, Cr, and Mn and their mixtures as B-site cations (Figure 3). Consistent with the general consensus in the literature, Figure 3 shows that the largest effects on the activation overpotentials stem from variations in the B-site cation with Fe-based perovskites, leading to the highest current densities and lowest non-Ohmic electrode polarization resistances at 1.2 V (yellow region). The reported non-Fe-based perovskites in general exhibit inferior electrochemical current densities (green region in Figure 3). Among non-Fe-based perovskites, $La_xSr_{1-x}TiO_{3+\delta}$ and $La_xSr_{1-x}Cr_yMn_{1-y}O_{3+\delta}$ have been the most commonly investigated. Ti, Cr, and Mn are more oxophilic metal cations than Fe. Extrapolating from reported density functional theory (DFT) studies for CO_2 reduction on metal surfaces,[45] the reason for their lower performance in comparison to Fe-based oxides could be hypothesized to stem from poisoning of the oxophilic B-site cations by intermediates or increased barriers for oxygen defect formation. Another factor could be related to electronic conductivity; however, this would also be largely affected by changes in the A-site composition (i.e., doping lanthanides with Sr),[80] which is coupled with effects on oxygen defect concentration, making it difficult to discriminate between these effects. Because of the low performance and limited trends among these non-Fe-based perovskites, we focus the remainder of this section on Fe-based perovskites for CO_2 reduction.

To tune the performance of Fe-based perovskites, doping the A- and the B-sites with various cations has been used as a strategy.[28,30,53,55−67] Mizusaki et al.[81] showed that doping the La site with Sr in $LaFeO_3$ improved the electrochemical rates. This was associated with Sr increasing electron−hole concentration and straightening of the O−B−O bond, leading to improved orbital overlapping between the 3d orbital of the B-site and O 2p orbital,[82] enhancing both ionic and electronic conductivity. Figure 4a selectively highlights from Figure 3 the current densities and non-Ohmic electrode polarization resistances measured at 1.2 V for electrochemical CO_2 reduction on reported Fe-based perovskites with varying A-site (green region) and B-site compositions (purple region). These data show that varying the A-site composition among lanthanide cations (A = La, Pr, Gd) of pure Fe-based perovskites (Figure 4a, green area) has a limited effect on the electrochemical activity for CO_2 reduction. However, doping La with alkaline-earth-metal cations (i.e., Ca^{2+}, Sr^{2+}, and Ba^{2+}) leads to an increase in performance. This is consistent with the lower oxidation state of alkaline-earth metal-cations in comparison to La^{3+}, inducing oxygen defects in the structure, which have been suggested to play a role along with the transition-metal cations in binding and activating CO_2. For example, our recently reported DFT calculations[52] and the works of others[83,84] showed that oxygen surface vacancies adjacent to Fe B-site cations significantly contributed toward increasing the CO_2 binding strength and improving CO_2 electrolysis rates. We reported that the oxygen defects played an important role in the adsorption energetics of CO_2, which led to adsorption energies that were comparable to or greater than those on stoichiometric surfaces.[52] With respect to B-site doping, Figure 4a (purple region) shows that, in general, doping the Fe B-site of $La_{1-x}Sr_xFe_{1-y}B_yO_3$ oxides with transition-metal cations such as Cr, Mn, Co, Ni, Cu, Mo, V, Nb, and Ti leads to a decrease in the electrochemical performance, which trends with the decrease of the Fe content in the B-site of these perovskites.

Thus far, we have mainly discussed the current densities and non-Ohmic electrode polarization resistances at a given applied voltage (1.2 V) for CO_2 electrolysis in SOECs. However, it is also critical to evaluate the selectivity (Faradaic efficiency) toward CO production (Figure 4b). In general, CO Faradaic efficiencies above 80% are reported for all SOECs containing Fe-based perovskite cathodes independent of the composition, suggesting that Fe cations are directly involved in CO_2 reduction to CO. The deviation from 100% CO Faradaic efficiency has been associated with over-reduction of the oxides[52] or potential leaks in the reported cells.

Stability is another critical parameter for SOEC electrocatalysts. However, this has been largely underevaluated in the literature for electrochemical CO_2 reduction on perovskites. For example, doping La with alkaline-earth-metal cations, such as $Sr^{2+}$and Ba^{2+}, has generally been reported to lead to an increase in electrochemical performance; however, alkaline-earth-metal cations in perovskites have been shown to surface segregate,[85] which becomes more facile with an increase in ionic radius from Sr^{2+} to Ba^{2+}.[53] Among the limited reported stability studies, Wang et al. showed through chronoamperometric (constant voltage) experiments at 1.2 V and 800 °C for 30 h that SOECs containing $La_{0.6}Sr_{0.4}Fe_{0.95}Mo_{0.05}O_3$-based cathodes underwent a slight decrease in performance in the first 5 h, which then stabilized for the remainder of the testing.[55] A postreaction scanning electron microscopic (SEM) analysis indicated minimal microstructural changes over time; however, no obvious agglomeration or changes in the distribution of elements at the electrode−cathode interface were observed. In another study, Zhou et al. assessed the stability of SOECs containing $La_{0.5}Sr_{0.5}FeO_3$ (LSF) and $La_{0.5}Sr_{0.5}Fe_{0.95}V_{0.05}O_3$ (LSFV) cathodes without a diffusion barrier layer and reported 0.022% and 0.015% performance degradation after 20 h of chronoamperometry experiments at 1.2 V and 800 °C, respectively.[56] After the stability test, cross-sectional SEM mapping of the cells indicated that V-doping prevented surface Sr segregation and particle agglomeration, which resulted in a higher stability of the cell containing the LSFV cathode. However, delamination between the electrode/electrolyte interfaces was observed for both cells, which was identified as the dominant reason for the degradation of SOECs during stability tests at a constant applied potential.

3.2. Double Perovskites and Ruddlesden−Popper Oxides.

A few double perovskites and Ruddlesden−Popper (R-P) oxides have been investigated as cathode electrocatalysts for the electrochemical reduction of CO_2 in SOECs.[86−89] Among the double perovskites, $Sr_2Fe_{1.5}Mo_{0.5}O_{6-\delta}$ (SFM) showed potential as both the CO_2 (fuel) and oxygen electrode for reversible SOECs, since it displayed excellent redox stability and high conductivity in both reducing and oxidizing environments. The electronic structure of Fe/Mo and strongly hybridized Fe 3*d* and O 2*p* states in SFM led to electronic defects and oxygen vacancies, thereby exhibiting excellent electron−ion transport properties. Li et al. investigated SOECs containing a SFM cathode under pure CO_2 atmospheres at 800 °C and reported a current density of 0.450 A/cm^2 at 1.2 V, which was inferior to that of the previously reported cells containing Fe-based ABO_3 perovskites.[88]

Few studies have investigated R-P oxides as cathode electrocatalysts for CO_2 electrolysis in SOECs. Ling et al. examined the stability of R-P $Sr_3Fe_2O_{7-\delta}$ and showed that it decomposed completely at 800 °C under a pressure of 10^{-20} atm.[86] In another study, Huan et al. showed that R-P $SrEu_2Fe_2O_7$ demonstrated excellent stability within 260 h of operation under CO_2 electrolysis conditions because the substitution of Sr^{2+} in the rock-salt layer by Eu^{3+} significantly enhanced the structural stability at the expense of the oxygen vacancy concentration.[90] In the case of non-Fe based R-P oxides, Ishihara et al.[87] reported that first-series R-P $La_2NiO_{4+\delta}$ and $La_{1.8}Sr_{0.2}NiO_{4+\delta}$ oxides were not very active for electrochemical CO_2 reduction.

3.3. Exfoliated Nonstoichiometric Mixed Metal Oxides.

The reported performances of nonstoichiometric mixed metal oxides for CO_2 reduction, as detailed above, in general suggest that the electrochemical rates can be tuned via changes in their cation composition; however, these rates are still largely lower than those reported for the state-of-the-art Ni/YSZ-based SOECs. An alternative approach to oxide compositional variations that has been used to enhance the CO_2 electrolysis rates is the *in situ* exsolution of the B-site cations leading to the formation of metal nanoparticles (NPs) on the surface of the mixed metal oxides under reducing conditions.[68,72,91−106] For a subset of oxides, it has been shown that CO_2 electrolysis rates on exfoliated oxides are generally higher than those on the parent oxide. For example, Liu et al. showed that exfoliated Fe nanoparticles from $LaSrFeO_{4+\delta}$ led to higher electrochemical rates for CO_2 reduction in comparison to the parent oxide.[93] In other works, Li et al. showed that exfoliation of NiFe alloy NPs from $Sr_{1.9}Fe_{1.5}Mo_{0.4}Ni_{0.1}O_{6-\delta}$ (SFM) led to significantly higher electrochemical CO_2 reduction rates as compared to the parent SFM oxide.[95] The increase in performance was linked to the improved surface kinetics for CO_2 reduction on the exfoliated NiFe alloy NPs at the interface with the oxide. A high CO Faradaic efficiency of 99.2% at 1.2 V and 800 °C was also reported. They showed that the exfoliated system exhibited long-term stability for 500 h under CO_2 reduction conditions due to the resistance from sintering and coking induced by the close interface between the exfoliated alloy NPs and the restructured surface of the parent oxide.

Figure 5 shows a summary of the tabulated current densities of reported SOECs containing exfoliated mixed metal oxide cathode electrocatalysts at an applied voltage of 1.2 V and 800 °C. In general, SOECs containing exfoliated monometallic Ni NPs from oxides have been reported to exhibit lower performances compared to those of exfoliated Fe- or Co-based monometallic systems (Figure 5, purple region). These activity trends are consistent with those reported and predicted from DFT for metal nanoparticles, which trended with the binding strength of oxygen on the metal surface (oxophilicity of the metal).[45,46] However, unlike metal-supported electrodes, the exfoliated systems have in general been reported to be more resistant to sintering and coking due to the close, enveloping interface with the restructured surface of the parent oxide.[107] In the case of exfoliated alloys (blue region in Figure 5), Fe-Ni alloys have been largely studied. Significant discrepancies in the performance of these systems exist potentially due to variations in the surface structure of the exfoliated alloys induced by the differences in the composition of the parent oxide and/or exfoliation conditions.

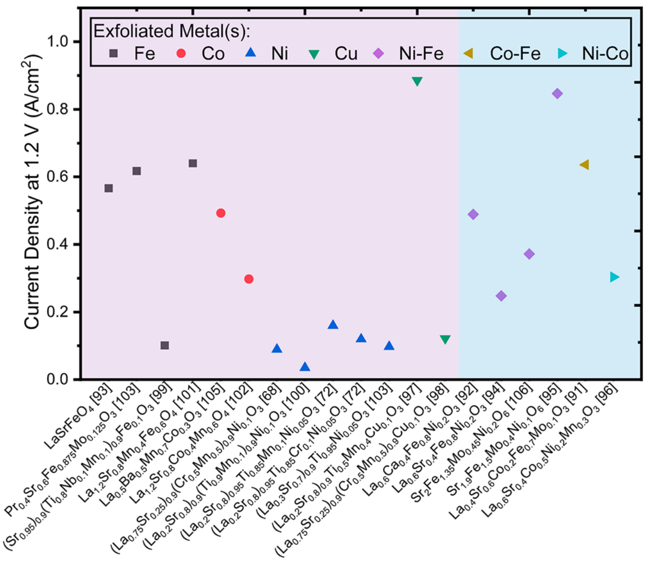

Figure 5. Current densities (absolute values) of SOECs containing exfoliated mixed metal oxide cathode electrocatalysts at an applied voltage of 1.2 V and 800 °C. The highlighted purple region represents monometallic NPs exfoliated from the parent oxide, while the blue region represents exfoliated alloy systems.

4. MECHANISTIC INSIGHTS ON CO_2 REDUCTION OVER NONSTOICHIOMETRIC MIXED METAL OXIDE ELECTROCATALYSTS

4.1. Experimental Studies.

Limited experimental studies exist on understanding the underlying mechanisms that govern CO_2 reduction on mixed metal oxide surfaces in SOECs. Opitz et al.[83] investigated the surface chemistry of $La_{0.6}Sr_{0.4}FeO_{3-\delta}$ electrodes during electrochemical CO_2 reduction by using near-ambient-pressure X-ray photoelectron spectroscopy (NAP-XPS) at SOEC operating temperatures. A sketch of the cell designed for these spectroscopic studies is shown in Figure 6a. These experiments showed that a bidentate $(CO_3)^{\bullet 3-}$ adsorbate was the key intermediate from CO_2 activation on $La_{0.6}Sr_{0.4}FeO_{3-\delta}$ electrodes (Figure 6b).

The concentration of this intermediate increased with increasing oxygen vacancy concentration in the oxide (induced through A-site doping), suggesting that surface oxygen vacancies were the predominant adsorption sites for CO_2. The reduction of the carbonate intermediate to CO was found to be the rate-limiting step. Two pathways for the formation of the bidentate carbonate intermediate were proposed based on the mode of CO_2 adsorption: one involved CO_2 adsorption via an oxygen vacancy on the surface of the perovskite coupled with electron transfer from a near-surface polaron, while the other involved a single charged surface oxygen vacancy where the carbonate intermediate formed by CO_2 binding on the vacancy and its coordination with an adjacent surface lattice oxygen ion. These studies suggested that formation of the bidentate carbonate intermediate was highly dependent on the

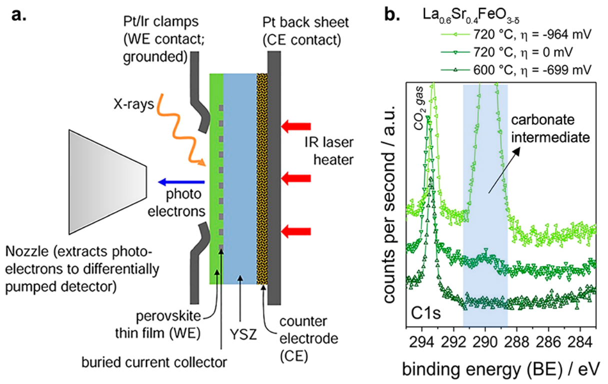

Figure 6. (a) Sketch (cross section) of an electrolysis cell mounted for NAP-XPS measurements. (b) Formation of a carbonate intermediate during CO_2 reduction on the LSF electrode at 600 and 720 °C in 0.25 mbar CO_2 at various cathodic polarizations (η) as detected by NAP-XPS. Reproduced from ref 83. Copyright 2017 American Chemical Society.

perovskite composition and surface termination due to the variations that these factors would induce on the arrangement/distance of two surface oxygen lattice sites.

4.2. Theoretical Studies.

4.2.1. Structural Models and Computational Methods.

Although there has been some recent work regarding the interaction of CO_2 and YSZ,[108] there exist only a limited number of reports regarding the reduction of CO_2 in SOECs with perovskite-based electrocatalysts.[50,109] The reported literature often assumes that the bulk of the ABO_3 structures is cubic,[110,111] even though this bulk structure is not what is observed experimentally for many perovskite structures.[112] One reason the cubic structure is used for these types of systems is the computational expense that is associated with the bulk structures observed experimentally, since the unit cell size is considerably larger. A natural question would be whether there is an influence on the reported results if one would use the same bulk structure as what is reported experimentally. In the studies that we discuss in the next subsection regarding CO_2 activation, the cubic unit cell was used in all but one study.[52]

Only a few of the studies related to CO_2 electrochemical reduction on perovskites delve deep into the mechanism utilizing transition state theory and determination of kinetic barriers.[43,44,52] In general, theoretical studies concerning the mechanism have focused mainly on the effects of oxygen vacancies[52,113,114] on the activation of CO_2 on the surface, with some investigations also probing the effect of supported heterogeneous nanoparticles on the oxide.[28,49,115−118] Although there have been many studies on perovskite surfaces regarding the oxygen evolution and reduction reactions, we restrict ourselves to the studies that involved the activation of CO_2 in the next subsection.

4.2.2. Oxygen Vacancy and Oxide Compositional Effects.

Oxygen vacancies have been largely linked to the adsorption and activation of CO_2 on the surface of perovskite catalysts. Theoretical studies typically conclude that CO_2 reduction requires at least two oxygen vacancies on the surface.[44] DFT calculations showed that the nature of B-sites affected the oxygen vacancy formation rate, consequently affecting the CO_2 reduction mechanism. For example, for the $La_{0.4}Sr_{0.6}Co_{0.2}Fe_{0.7}Mo_{0.1}O_{3-\delta}$ system, a corresponding density of states analysis indicated that the B-sites were more reactive toward CO_2 activation than the A-sites due to the electronic states of the Fe B-site being closer to the Fermi energy, as shown in Figure 7a.[116] The influence of the B-site on the activation of CO_2 was recently elucidated experimentally and computationally on undoped La-based perovskites,[52] where the reactivities of $LaFeO_3(110)$, $LaCoO_3(001)$, and $LaNiO_3(001)$ toward CO_2 activation were compared in the absence of oxygen vacancies. Through a comparison of the measured diffuse reflectance infrared Fourier transform (DRIFT) spectra with the simulated infrared spectra (see Figure 7b), CO_2 was determined to adsorb in monodentate and bidentate configurations. On $LaFeO_3$ and $LaCoO_3$, CO_2 adsorbed via both monodentate and bidentate configurations. Conversely, in the case of $LaNiO_3$, CO_2 adsorption mainly occurred through a bidentate configuration. On a stoichiometric $LaFeO_3(001)$ surface, the adsorption strength of CO_2 was found to be weaker in comparison to $LaNiO_3(001)$ and $LaCoO_3(110)$, whereas in the presence of vacancies, the adsorption strength of CO_2 on $LaFeO_3(001)$ was greater than that on $LaNiO_3(001)$ and $LaCoO_3(110)$. Interestingly, the computational results indicated that the adsorption of CO_2 was activated on all three surfaces, as illustrated in Figure 7c for $LaCoO_3$. This study concluded that both the nature of the B-site and oxygen vacancy distribution must be considered to arrive at a predictive model for determining CO_2 reduction energetics on nonstoichiometric mixed metal oxides.

When considering the entire mechanism of CO_2 reduction on perovskite surfaces, the process is not fully understood,[44,119] with only a handful of DFT-based studies that consider the dissociative adsorption of CO_2.[43,44,52,54] Kozokaro et al. quantified the CO_2 reduction mechanism on $La_{0.3}Sr_{0.7}Fe_{0.7}Cr_{0.3}O_3$ using a DFT+U functional.[44] The proposed mechanism involved two surface oxygen vacancies as adsorption and activation sites for CO_2 on this perovskite surface. The corresponding barrier calculations revealed that the bond angle of gaseous CO_2 decreased from 171.47 to 124.94° when the CO_2 molecule adsorbed on the surface as a bidentate carbonate intermediate. The oxygen species of the CO_2 molecule adsorbed on a surface Fe cation near an oxygen vacancy site with the corresponding carbon adsorbing on the lattice oxygen. The oxidation state of the B-site was also altered when CO_2 chemisorbed. Due to its electronegative nature, Fe was found to not participate in the transfer of electrons in the reduction mechanism; instead, the oxidation state of the doped cation, Cr, changed from +4 to +5 by donating an electron to the carbon atom of the adsorbed CO_2. CO_2 was further reduced, as an oxygen species within the CO_2 molecule filled a nearby oxygen vacancy, while one of the electrons from the dissociated oxygen was donated to the newly formed CO molecule for which its desorption was thermally activated. This work highlighted the importance of doping the Fe B-site with Cr for CO_2 reduction, as surface Cr cations had a higher oxidation state than their bulk counterparts, increasing the rate of oxygen vacancy formation on the surface and thus increasing the reactivity of the catalyst toward CO_2 activation.

As was mentioned above, cation doping can be used to tune the rate of formation and stability of oxygen vacancies. Ren et al. constructed a DFT+U-based model on (001)FeO-terminated $La_{0.5}Sr_{0.5}FeO_3$ (LSF) with various amounts of Mn/Ni doping in the B-site.[43] Four configurations (pure LSF, Mn-doped LSF, Ni-doped LSF and LSF codoped with Ni and Mn) with four oxygen vacancies were tested using the proposed mechanism, for which all doping strategies were considered and where the CO_2 molecule adsorbed on a surface

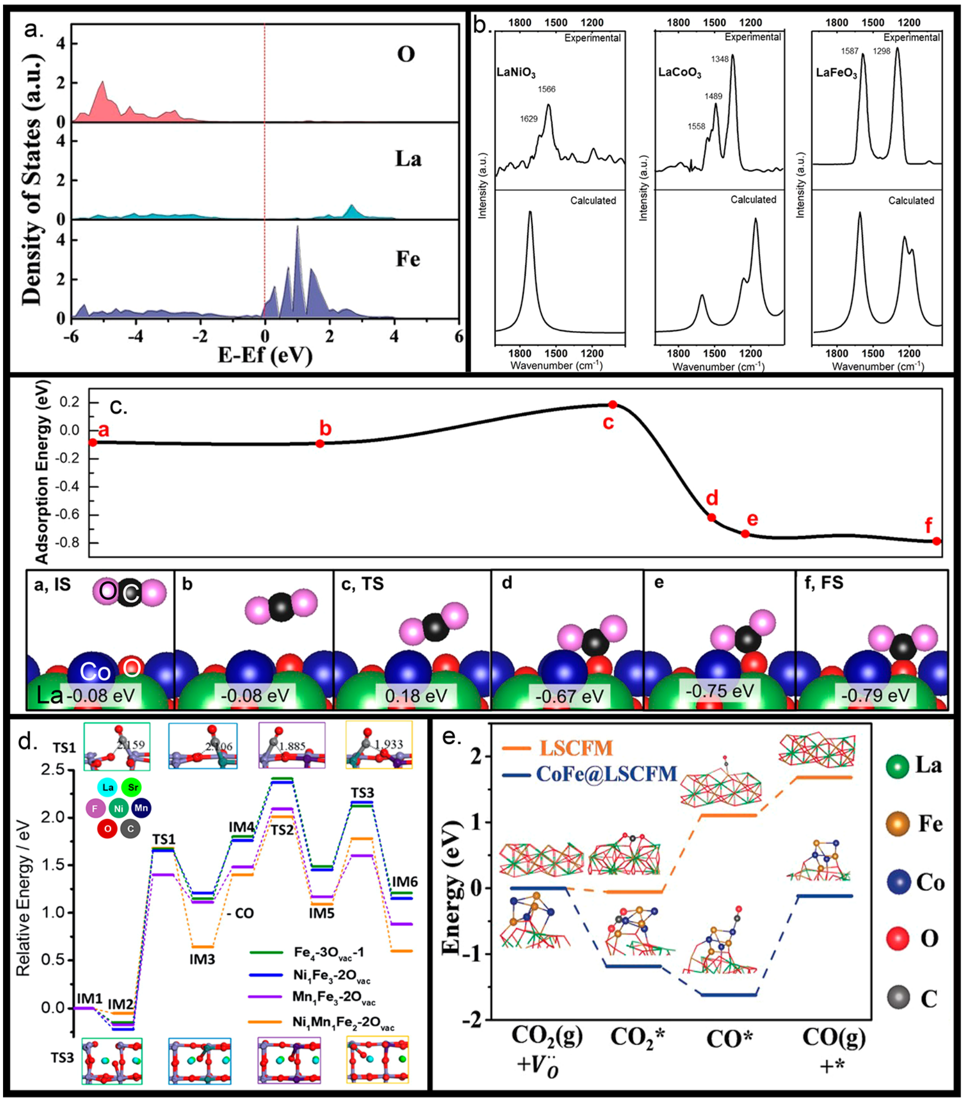

Figure 7. (a) The analysis of a $La_{0.4}Sr_{0.6}Co_{0.2}Fe_{0.7}Mo_{0.1}O_{3-\delta}$ perovskite surface. The red dashed line indicates the Fermi energy level. Reproduced with permission from ref 116. Copyright 2020 John Wiley and Sons. (b) DRIFTS spectra of $LaNiO_3$, $LaCoO_3$, and $LaFeO_3$. In the cases where multiple possible configurations were present within the DFT-based model, the intensities of the IR peaks were averaged, and overall peaks were established. Reproduced with permission from ref 52. Copyright 2022 IOP Publishing. (c) Nudged elastic band calculation for the adsorption of CO_2 on $LaCoO_3$. CO_2 adsorbs in a bidentate configuration with an adsorption energy of −0.79 eV. The atoms are marked as follows: La in green, Co in dark blue, surface O in red, O from CO_2 in purple, and C from CO_2 in black. Reproduced with permission from ref 52. Copyright 2022 IOP Publishing. (d) Potential energy surface for CO_2 reduction and oxygen migration through the surface for four different models: pure LSF, LSF with Ni doping, LSF with Mn doping, and LSF codoped with Mn and Ni. Images on the top and bottom correspond to the transition states when the CO_2 adsorbs and when oxygen is integrated into the surface, respectively, on each of the surfaces indicated by the color surrounding the image corresponding to the line within the plot. The initial state is the reference energy for all surfaces. The atoms are marked as follows: La in cyan, Sr in lime green, Fe in purple, Ni in teal, Mn in dark blue, O in red, and C in gray. Reproduced with permission from ref 43. Copyright 2020 Elsevier. (e) Potential energy surface for CO_2 electrolysis with and without an adsorbed CoFe cluster. V_O indicates the presence of an oxygen vacancy. CO_2* indicates adsorbed CO_2, and CO* indicates adsorbed CO on the surface. The atoms are marked as follows: La in green, Fe in copper, Co in blue, O in red, and C in black. Reproduced with permission from ref 116. Copyright 2020 John Wiley and Sons.

B-site cation near an oxygen vacancy. When it adsorbed on the pure LSF surface, the adsorption strength of CO_2 was −0.15 eV, while it was −0.05 eV on LSF codoped with Ni and Mn. In all configurations, the adsorption of CO_2 was activated, forming a bidentate intermediate with the carbon atom adsorbed on a lattice oxygen species and with one of the oxygen atoms within the CO_2 molecule binding to an Fe cation. Reduction of CO_2 was the rate-limiting step for all surfaces shown in Figure 7d. It was found that doping with only Mn led to the lowest energy barrier: however, at the cost of lattice stability toward the formation of oxygen vacancies. Codoping with Mn and Ni was hypothesized to increase the concentration of oxygen vacancies. Yang et al. modeled a very similar surface, the energetically more favorable LaSrFeO-terminated $La_{0.75}Sr_{0.25}FeO_3(110)$ surface with one surface oxygen vacancy, using DFT.[54] Barrier calculations revealed that the CO_2 molecule adsorbed in a bidentate configuration with the carbon atom of CO_2 adsorbing on a lattice oxygen and the oxygen species from the CO_2 molecule adsorbing on La and Sr A-sites. In this configuration, CO_2 interacted strongly with the surface with an adsorption energy of −0.85 eV. The dissociative adsorption of CO_2 had a high energy barrier of

1.43 eV and was the rate-limiting step.[54] Once CO was formed and the remaining oxygen integrated into the surface, CO then desorbed. Limited information was provided in this study regarding the role of oxygen vacancies in the reduction of CO_2 and the specifics surrounding electron transfer to understand the role of the A-site on CO_2 adsorption.

Oxygen surface vacancy formation through oxygen mobility within the perovskite surface has also been considered as a potential rate-limiting step, depending on the oxide composition and structure. The local coordination around the oxygen vacancies in these oxides involves both the B-site and the A-site cations, which affect oxygen migration.[114] Doping of the A- and B-sites has been used as a strategy to enhance oxygen migration through the stabilization of the surface vacancies and destabilization of subsurface oxygen vacancies.[43] Highly oxophilic B-site cations have shown to limit the oxygen migration through the surface and lower the oxygen vacancy formation rate by stabilizing oxygen within the surface.[44] Mastrikov et al. studied bulk $La_{1-x}Sr_xCo_{1-y}Fe_yO_3$ with oxygen vacancies and found that the migration of oxygen vacancies was affected by the B-site cation with Co, leading to lower oxygen migration barriers than for Fe.[114] An optimal oxygen vacancy concentration is required to enhance CO_2 reduction rates, since a high concentration of oxygen vacancies in the oxide surface can lead to (i) a deficiency of electrons on the surface, reducing the charge transfer between the surface and CO_2 and thus reducing the production of CO,[49] and/or (ii) surface destabilization, causing cation segregation and loss of active sites.[116]

4.2.3. Surface Cluster Models Mimicking Exfoliated Oxides. Surface activity toward the reduction of CO_2 can also be augmented by decorating the perovskite with NP clusters as in the exfoliating/exsolved systems discussed above. Ye et al. modeled the $SrTiO_3(110)$ surface on which a Ni NP was adsorbed.[118] Without surface oxygen vacancies, CO_2 adsorbs in a bidentate configuration at the Ni cluster and surface interface. The bond length between the carbon and the Ni cluster was a meager 1.906 Å, explaining the high adsorption energy of −2.6 eV. A charge density calculation suggested that the interactions between the 2*p* orbitals of C, O, and Ni stimulated the adsorption of CO_2. Surface defects introduced near the Ni cluster promoted exothermic CO_2 activation. In this case, CO_2 adsorption occurred through carbon binding on Ni and one oxygen integrating into a surface oxygen vacancy, as indicated by near-bulk bond lengths between the oxygen and the surrounding Sr and Ti.[118] In the charge density calculations, the Ni 4*s* orbital was depleted due to the filling of the C 2*p* and O 2*p* orbitals that occurred because the C−O bond was broken during adsorption. These results suggested that oxygen vacancies and the Ni cluster acted synergistically to improve CO_2 reduction. However, the activation barrier was not quantified. Yang et al. also studied $SrTiO_3$ when a Cu NP was deposited on the surface.[117] The addition of the NP on the surface reduced the oxygen vacancy formation energy from 3.55 to 3.42 eV, hinting that the NP promoted their formation. The Cu NP and the $SrTiO_3$ interface activated CO_2 by decreasing the free energy barrier from 1.38 to 0.82 eV.

In another study that was previously discussed in this review, Lv et al. modeled $La_{0.4}Sr_{0.6}Co_{0.2}Fe_{0.7}Mo_{0.1}O_{3-\delta}$ with CoFe alloy NPs decorating the surface to mimic exsolved/exfoliated oxide systems.[116] Experimentally, heterogeneous NPs were generated on the surface by introducing an A-site deficiency in the oxide. On analysis using DFT calculations (Figure 7e), the addition of a CoFe cluster ($CoFe@La_{0.4}Sr_{0.6}Co_{0.2}Fe_{0.7}Mo_{0.1}O_{3\text{-}\delta}$) changed the tridentate adsorption of CO_2 on the surface from a physisorbed configuration to a chemisorbed configuration by strengthening the adsorption energy from −0.1 to −1.2 eV. This enhanced reactivity correlated well with a corresponding density of states analysis for $CoFe@La_{0.4}Sr_{0.6}Co_{0.2}Fe_{0.7}Mo_{0.1}O_{3-\delta}$, which demonstrated that the exsolved Co and Fe in $CoFe@La_{0.4}Sr_{0.6}Co_{0.2}Fe_{0.7}Mo_{0.1}O_{3-\delta}$ had richer electronic states around the Fermi level than the those depicted for $La_{0.4}Sr_{0.6}Co_{0.2}Fe_{0.7}Mo_{0.1}O_{3-\delta}$ in Figure 7a. CO_2 activated on the surface of a CoFe cluster due to the high concentration of electrons localized by the cluster. On the clean surface, the dissociation of CO_2 on the catalyst was the rate-limiting step, whereas the desorption of CO was the rate-limiting step when the surface was decorated with a CoFe cluster. These theoretical studies suggest that significant differences exist in the CO_2 reduction mechanism and energetics between the exfoliated and parent oxides.

5. SUMMARY AND OUTLOOK

In this review, we summarize the effects from the composition and oxygen deficiency of nonstoichiometric mixed ionic and electronic conducting oxide electrocatalysts on the electrochemical reduction of CO_2 in SOECs by combining the insights from experimental and theoretical studies reported in the literature. In general, the A-site cations in these oxides do not directly contribute to CO_2 activation; however, A-site dopants have been used to increase the concentration of oxygen surface defects, which have been suggested to assist in the adsorption of CO_2. On the other hand, the nature of the B-site cations in these oxides directly contributes to C−O bond activation in CO_2 and affects the activation overpotentials. Oxides containing Fe B-site cations have been shown to lead to the highest reported electrochemical rates for CO_2 reduction in SOECs. Exfoliation of metal NPs from the B-site cations of nonstoichiometric mixed metal oxides has been reported as an effective approach to improve the electrochemical rates of CO_2 reduction, through inducing changes in the mechanism and the energetics of this process.

Fundamental studies in understanding the mechanism of CO_2 reduction on nonstoichiometric mixed metal oxides are critical toward devising ways of improving the electrochemical performance of these oxides for CO_2 reduction. DFT calculations typically suggest that the rate-limiting step for CO_2 reduction is the adsorption or activation of CO_2 on the surface, depending on the oxide composition. By utilizing both surface oxygen vacancies and exfoliated NP clusters, the surface can be altered to improve the reaction kinetics.

Proper evaluation of the reported electrocatalysts for CO_2 reduction in SOECs is significantly challenged by the lack of standardized benchmarking protocols to characterize the electrocatalysts and investigate their catalytic performance. For example, Figure 8 shows that variations in the performance of SOECs containing the same cathode electrocatalyst are significant among the various reported studies. This can stem from variations in the structures of the cell and the electrocatalyst induced by differences in the synthesis, along with variations in the reaction conditions. To address this challenge, benchmarking protocols for determining and reporting the electrochemical performance along with detailed electrocatalyst characterization would be necessary. Variations in electrocatalyst synthesis can significantly affect the oxide

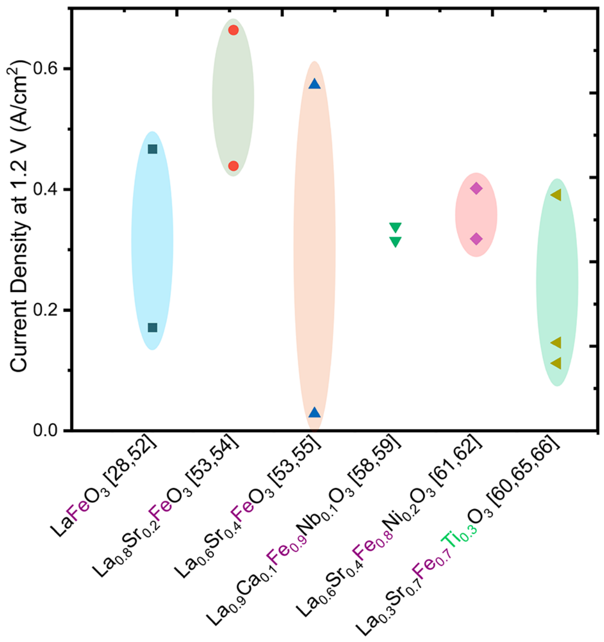

Figure 8. Variations in reported current densities (absolute values) of SOECs containing the same cathode electrocatalysts at an applied voltage of 1.2 V and an operating temperature of 800 °C.

defect concentration and the surface oxide composition, termination, and surface area, which ultimately influence catalytic reactivity. Thus, benchmarking protocols for characterizing the electrocatalyst structure and, especially, the surface structure should be developed. These should include oxide characterization using X-ray diffraction for a bulk crystal structure determination, iodometric titration for quantification of bulk oxygen defect concentration, scanning and high-resolution transmission electron microscopy along with elemental mapping for determining particle size/geometry and A/B site cation distribution, and X-ray photoelectron spectroscopy for measuring the oxidation state of cations in the oxide's near-surface region. Electrocatalyst characterization should be reported before and after electrochemical testing using some of these methods. In the case of protocols for evaluation of the electrocatalytic performance, they should include a range of temperatures (e.g., 500−800 °C) and gas compositions of pure CO_2 and CO_2 mixed with small amounts of CO (1−5%) to establish an open-circuit potential that can be used to identify potential problems with the cell prior to testing. The residence time is another parameter which is often neglected that should be reported to understand potential variations in CO_2 conversions. Normalization of the rates per surface area of the oxides (measured, for example, via N_2 physisorption−Brunauer, Emmett, and Teller (BET) surface area) should also be reported, since this is the catalytically active surface for this reaction. Electrochemical impedance spectroscopy (EIS) is a useful technique for differentiating variations in Ohmic versus non-Ohmic resistances of SOECs; however, it is often not reported. Fitting the EI spectra to an equivalent circuit model should be considered to determine resistances associated with interfacial charge transfer and related processes. The activation energy for these processes can also be extrapolated using an Arrhenius plot of the specific non-Ohmic electrode polarization resistances as a function of temperature.[120] Continuum-based models that attempt to describe impedance in terms of chemical processes (bulk diffusion and surface reaction kinetics) have also been developed; however, such models have had limited applications to these specific systems.[121]

Generally, the largely reported potential/current behaviors of full SOECs can only evaluate the overall cell performance for this process. An explicit analysis of the elementary steps is essential to gain an understanding of the underlying mechanism of CO_2 reduction, as well as to determine the rate-limiting step, which is quite challenging. Toward this, combining electrochemical measurements with *in situ*/*operando* characterization studies and theoretical calculations is critical in providing fundamental insights for CO_2 reduction.[122] *In situ* and *operando* methods are being developed to address these issues and are beginning to provide fundamental insights into solid oxide electrochemical cell processes. For example, *in situ* Raman spectroscopy was used to acquire vibrational spectra from solid oxide fuel cell (SOFC) anodes at 715 °C under operating conditions to investigate the appearance and disappearance of different carbonaceous species on the electrode surfaces.[123,124] Furthermore, *in situ* X-ray absorption spectroscopic (XAS) experiments have been performed to obtain information on the chemical state of SOFC electrodes under electrochemical conditions. For instance, these studies facilitated an understanding of the effect of changes of environmental conditions, such as temperature, partial pressure of O_2, and electric potential, on the chemical state of manganese in the $La_{0.5}Sr_{0.5}MnO_{3\pm\delta}$ catalyst.[125] On the other hand, near-ambient-pressure X-ray photoelectron spectroscopy (NAP-XPS) was used as a primary technique to resolve the potential-dependent evolution of different intermediate species on the surface of electrodes, local surface potentials, electrochemically active regions, and shifts in surface oxidation states in operating SOECs.[83,126,127] Similar approaches are critical for obtaining a detailed mechanistic understanding of CO_2 reduction on oxide-based SOEC cathodes.

There have been limited studies conducted using theoretical calculations to investigate the CO_2 reduction mechanism on mixed metal oxide surfaces. Nonstoichiometric mixed ionic and electronic conducting oxides are complex structures, and exploring the electronic properties of the surface using theory provides an important pathway for understanding the underlying CO_2 reduction mechanism. Experimental work varies based on environmental factors, and although theoretical calculations are consistent, first-principles-based simulations need reliable levels of theory that take into account the experimental realities in order to be predictive. Inconsistencies in the literature are often related to the level of theory that was used, which is an additional challenge to accurately describe these systems. The DFT+U method has often been utilized to elucidate the underlying electronic structure of nonstoichiometric mixed metal oxides (i.e., perovskites). However, as can be seen in Figure 9, such a level of theory has only been used in three of the seven studies of that were overviewed in this paper. To improve current theoretical studies, one needs to determine how the level of theory affects the transition state calculations toward CO_2 activation.

Further, even the accuracy of the reported DFT+U studies that were surveyed in this review (see Figure 9) is uncertain since the value of U_{eff} will change as one changes the geometry of the system and needs in principle to be calculated self-consistently.[128] However, neither of the DFT+U studies that were presented in this review calculated the value of U_{eff} self-

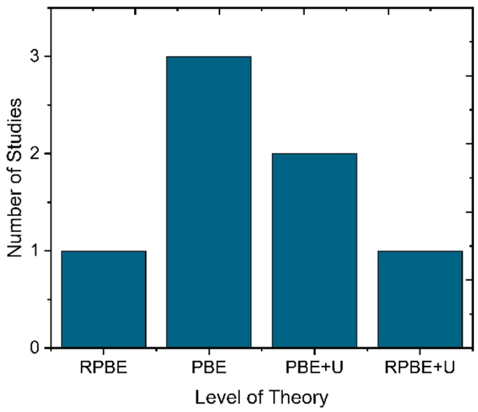

Figure 9. Overview of the levels of theory (RPBE,[52] PBE,[54,114,118] RPBE+U,[116] and PBE+U[43,44]) that were used in theoretical studies involving the activation of CO_2 on perovskite-based catalysts.

consistently. They use a value, for example, of $U_{\mathrm{eff}} = (U - J) =$ 4 eV for Fe (where U describes the Coulomb on-site integrals and J describes the repulsion between opposite spin electrons[129]) in both $La_{0.3}Sr_{0.7}Fe_{0.7}Cr_{0.3}O_3$ (LSFCr) and $La(Sr)FeO_3$ based on the fact that such a value of U_{eff} is the one that is needed to get the correct band gap for the bulk FeO_x system.[130] However, such a U_{eff} value has been shown to not get the correct trends for the formation of oxygen vacancies in Fe_2O_3 in comparison to experiment.[131] This is one of the reasons some research groups opt to use a standard generalized gradient approximation functional rather than utilize the DFT+U method with a fixed value of U_{eff}. Alternative approaches that do not involve the self-consistent calculation of the U value would be to use either the SCAN functional[132] or the HSE06 functional,[133] although there is an additional computational expense when the HSE06 functional is used for periodic systems if a plane wave basis set (such as is the case with VASP) is used. As such, other first-principles-based codes that do not use a plane wave basis set, such as the CRYSTAL code,[134] should be considered. Theoretical calculations are critical toward obtaining an understanding of the elementary step mechanism of CO_2 reduction on these oxides; however, they are currently underutilized, potentially due to the complexity of these systems. Thus, it is critical that theoretical calculations are benchmarked with experimental studies to determine reliable underlying energetics and mechanism for CO_2 reduction.

Another example in which the experimental complexities are not accounted for in the underlying computational models is with regard to the influence of external electric fields, which are present within a SOEC environment. Recent experimental work by Kubiak and co-workers have quantified the strength of interfacial electric fields on functionalized Au electrodes at the interface with a liquid electrolyte using sum frequency generation spectroscopy and correlated their results with the simulation of such spectra, where interfacial electric fields on the order of 0.1 V/Å were determined to be present.[135] Electric fields of this strength were shown to significantly influence CO_2 binding.[135] Although these experiments were performed at liquid electrolyte−solid electrode interfaces, which are clearly beyond the scope of the current review, it highlights the effect of electric fields generated at electrified interfaces on CO_2 reduction, which is often neglected. An external electric field was also shown within a DFT-based model to facilitate the activation of CO_2 on YSZ, where a negative electric field of −1.0 V/Å resulted in the chemisorption of CO_2 through the formation of a carbonate species.[108] Unlike the activated adsorption illustrated in Figure 7 for CO_2 on $LaCoO_3$, the formation of a carbonate species seemed to be barrierless on YSZ when an electric field of −1.0 V/Å was applied.[108] Thus, the incorporation of electric field effects should be considered in studying the energetics of electrochemical CO_2 reduction on mixed metal oxide SOEC cathodes, since the presence of an electric field might reduce the barrier for CO_2 chemisorption on perovskite-based catalysts and thus might be a more accurate representation of the energetics at the electrochemical interfaces of SOECs.

Further, in order to consider the high temperatures that are involved in a SOEC environment, one can use *ab initio* molecular dynamics. However, such an approach is a challenge in practice given the limited time scales and length scales that one can access with such a level of theory. As such, some researchers have utilized, for example, classical molecular dynamics simulations with charge optimized many-body empirical potentials[136] or reactive molecular dynamics[137] to overcome such limitations. Finally, the presence of defects, such as oxygen vacancies, have been underexplored within first-principles-based models, but experimental studies exemplify that surface oxygen defects are a determining factor in the overall reaction.

The failure to model the phenomena occurring in experimental studies limits the usefulness of the theoretical data. Theory provides an important pathway to explore the trends associated with mixed oxide systems for CO_2 reduction. Trend data concerning the effects of electric field strength or oxygen vacancy concentration over a wide range of perovskite compositions could inform experimental studies on the conditions that promote higher catalytic activity on mixed metal oxide surfaces. For the most part, however, the theoretical papers discussed in this review are varied and limited enough that identifying trends is relatively difficult. Future theoretical studies focusing on trend data would enhance the overall understanding of the influential electronic properties required for enhancing the rate of CO_2 reduction to better inform the experimental studies.

■ AUTHOR INFORMATION

Corresponding Authors

Eranda Nikolla − *Department of Chemical Engineering and Materials Science, Wayne State University, Detroit, Michigan 48202, United States; Department of Chemical Engineering, University of Michigan, Ann Arbor, Michigan 48109, United States;* orcid.org/0000-0002-8172-884X; Email: erandan@umich.edu

Jean-Sabin McEwen − *The Gene & Linda Voiland School of Chemical Engineering and Bioengineering, Department of Physics and Astronomy, Department of Chemistry, and Department of Biological Systems Engineering, Washington State University, Pullman, Washington 99164, United States; Institute for Integrated Catalysis, Pacific Northwest National Laboratory, Richland, Washington 99352, United States;* orcid.org/0000-0003-0931-4869; Email: js.mcewen@wsu.edu

Reinhard Denecke − *Wilhelm-Ostwald Institute for Physical and Theoretical Chemistry, Leipzig University, 04103 Leipzig, Germany;* orcid.org/0000-0003-1065-5791; Email: denecke@uni-leipzig.de

Authors

Elif Tezel − *Department of Chemical Engineering and Materials Science, Wayne State University, Detroit, Michigan 48202, United States*

Ariel Whitten − *The Gene & Linda Voiland School of Chemical Engineering and Bioengineering, Washington State University, Pullman, Washington 99164, United States*

Genevieve Yarema − *Department of Chemical Engineering and Materials Science, Wayne State University, Detroit, Michigan 48202, United States;* orcid.org/0000-0003-2524-7301

Complete contact information is available at: https://pubs.acs.org/10.1021/acscatal.2c03398

Author Contributions

E.T. and A.W. contributed equally.

Notes

The authors declare no competing financial interest.

■ ACKNOWLEDGMENTS

The authors acknowledge the primary financial support from the National Science Foundation Ceramics Program (Award Numbers DMR-1929314 and DMR-1929306). The Pacific Northwest National Laboratory is operated by Battelle for the U.S. DOE.

■ REFERENCES

(1) Hoegh-Guldberg, O.; Jacob, D.; Taylor, M.; Guillén Bolaños, T.; Bindi, M.; Brown, S.; Camilloni, I. A.; Diedhiou, A.; Djalante, R.; Ebi, K.; Engelbrecht, F.; Guiot, J.; Hijioka, Y.; Mehrotra, S.; Hope, C. W.; Payne, A. J.; Pörtner, H.-O.; Seneviratne, S. I.; Thomas, A.; Warren, R.; Zhou, G. The human imperative of stabilizing global climate change at 1.5°C. *Science* **2019**, *365* (6459), No. eaaw6974.

(2) Bui, M.; Adjiman, C. S.; Bardow, A.; Anthony, E. J.; Boston, A.; Brown, S.; Fennell, P. S.; Fuss, S.; Galindo, A.; Hackett, L. A.; Hallett, J. P.; Herzog, H. J.; Jackson, G.; Kemper, J.; Krevor, S.; Maitland, G. C.; Matuszewski, M.; Metcalfe, I. S.; Petit, C.; Puxty, G.; Reimer, J.; Reiner, D. M.; Rubin, E. S.; Scott, S. A.; Shah, N.; Smit, B.; Trusler, J. P. M.; Webley, P.; Wilcox, J.; Mac Dowell, N. Carbon capture and storage (CCS): the way forward. *Energy Environ. Sci.* **2018**, *11* (5), 1062−1176.

(3) Ho, H.-J.; Iizuka, A.; Shibata, E. Carbon capture and utilization technology without carbon dioxide purification and pressurization: A review on its necessity and available technologies. *Ind. Eng. Chem. Res.* **2019**, *58* (21), 8941−8954.

(4) Gao, W.; Liang, S.; Wang, R.; Jiang, Q.; Zhang, Y.; Zheng, Q.; Xie, B.; Toe, C. Y.; Zhu, X.; Wang, J.; Huang, L.; Gao, Y.; Wang, Z.; Jo, C.; Wang, Q.; Wang, L.; Liu, Y.; Louis, B.; Scott, J.; Roger, A.-C.; Amal, R.; He, H.; Park, S.-E. Industrial carbon dioxide capture and utilization: state of the art and future challenges. *Chem. Soc. Rev.* **2020**, *49* (23), 8584−8686.

(5) Jhong, H.-R. M.; Ma, S.; Kenis, P. J. A. Electrochemical conversion of CO_2 to useful chemicals: current status, remaining challenges, and future opportunities. *Curr. Opin. Chem. Eng.* **2013**, *2* (2), 191−199.

(6) Saravanan, A.; Senthil Kumar, P.; Vo, D.-V. N.; Jeevanantham, S.; Bhuvaneswari, V.; Anantha Narayanan, V.; Yaashikaa, P. R.; Swetha, S.; Reshma, B. A comprehensive review on different approaches for CO_2 utilization and conversion pathways. *Chem. Eng. Sci.* **2021**, *236*, 116515.

(7) Martín, A. J.; Larrazábal, G. O.; Pérez-Ramírez, J. Towards sustainable fuels and chemicals through the electrochemical reduction of CO_2: lessons from water electrolysis. *Green Chem.* **2015**, *17* (12), 5114−5130.

(8) Wang, G.; Chen, J.; Ding, Y.; Cai, P.; Yi, L.; Li, Y.; Tu, C.; Hou, Y.; Wen, Z.; Dai, L. Electrocatalysis for CO_2 conversion: from fundamentals to value-added products. *Chem. Soc. Rev.* **2021**, *50* (8), 4993−5061.

(9) Hu, B.; Guild, C.; Suib, S. L. Thermal, electrochemical, and photochemical conversion of CO_2 to fuels and value-added products. *J. CO_2 Util.* **2013**, *1*, 18−27.

(10) Galadima, A.; Muraza, O. Catalytic thermal conversion of CO_2 into fuels: Perspective and challenges. *Renew. Sust. Energy Rev.* **2019**, *115*, 109333.

(11) Ruiz-López, E.; Gandara-Loe, J.; Baena-Moreno, F.; Reina, T. R.; Odriozola, J. A. Electrocatalytic CO_2 conversion to C_2 products: Catalysts design, market perspectives and techno-economic aspects. *Renew. Sust. Energy Rev.* **2022**, *161*, 112329.

(12) Chen, J.; Wang, T.; Li, Z.; Yang, B.; Zhang, Q.; Lei, L.; Feng, P.; Hou, Y. Recent progress and perspective of electrochemical CO_2 reduction towards C_2-C_5 products over non-precious metal heterogeneous electrocatalysts. *Nano Res.* **2021**, *14* (9), 3188−3207.

(13) Abdelnaby, M. M.; Liu, K.; Hassanein, K.; Yin, Z. Photo/electrochemical carbon dioxide conversion into C_{3+} hydrocarbons: Reactivity and selectivity. *ChemNanoMat* **2021**, *7* (9), 969−981.

(14) Zhang, W.; Jin, Z.; Chen, Z. Rational-Designed principles for electrochemical and photoelectrochemical upgrading of CO_2 to value-added chemicals. *Adv. Sci. Lett.* **2022**, *9* (9), 2105204.

(15) Song, Y. F.; Zhang, X. M.; Xie, K.; Wang, G. X.; Bao, X. H. High-Temperature CO_2 electrolysis in solid oxide electrolysis cells: developments, challenges, and prospects. *Adv. Mater.* **2019**, *31* (50), 1902033.

(16) Gao, F.-Y.; Bao, R.-C.; Gao, M.-R.; Yu, S.-H. Electrochemical CO_2 to CO conversion: electrocatalysts, electrolytes, and electrolyzers. *J. Mater. Chem. A* **2020**, *8* (31), 15458−15478.

(17) Bertleff, W.; Roeper, M.; Sava, X. Carbonylation. In *Ullmann's encyclopedia of industrial chemistry*; Wiley: 2012; pp 3269−3294.

(18) Bierhals, J. Carbon Monoxide. In *Ullmann's encyclopedia of industrial chemistry*; Wiley: 2012; pp 3253−3268.

(19) Reutemann, W.; Kieczka, H., Formic Acid. In *Ullmann's encyclopedia of industrial chemistry*; Wiley: 2012; pp 8200−8221.

(20) Weststrate, C. J.; van de Loosdrecht, J.; Niemantsverdriet, J. W. Spectroscopic insights into cobalt-catalyzed Fischer−Tropsch synthesis: A review of the carbon monoxide interaction with single crystalline surfaces of cobalt. *J. Catal.* **2016**, *342*, 1−16.

(21) Chen, P.-P.; Liu, J.-X.; Li, W.-X. Carbon monoxide activation on cobalt carbide for Fischer−Tropsch synthesis from first-principles theory. *ACS Catal.* **2019**, *9* (9), 8093−8103.

(22) Küngas, R. Review-Electrochemical CO_2 reduction for CO production: comparison of low- and high-temperature electrolysis technologies. *J. Electrochem. Soc.* **2020**, *167* (4), 044508.

(23) Hauch, A.; Küngas, R.; Blennow, P.; Hansen, A. B.; Hansen, J. B.; Mathiesen, B. V.; Mogensen, M. B. Recent advances in solid oxide cell technology for electrolysis. *Science* **2020**, *370* (6513), No. eaba6118.

(24) Ebbesen, S. D.; Jensen, S. H.; Hauch, A.; Mogensen, M. B. High temperature electrolysis in alkaline cells, solid proton conducting cells, and solid oxide cells. *Chem. Rev.* **2014**, *114* (21), 10697−10734.

(25) Gu, X. K.; Carneiro, J. S. A.; Nikolla, E. Heterogeneous electrocatalysts for CO_2 reduction. *Royal Society of Chemistry; Catalysis* **2017**, *29*, 94−121.

(26) Sakai, N.; Horita, T.; Yamaji, K.; Brito, M. E.; Yokokawa, H.; Kawakami, A.; Matsuoka, S.; Watanabe, N.; Ueno, A. Interface stability among solid oxide fuel cell materials with perovskite structures. *J. Electrochem. Soc.* **2006**, *153* (3), A621−A625.

(27) Huang, K.; Feng, M.; Goodenough, J. B.; Schmerling, M. Characterization of Sr-Doped $LaMnO_3$ and $LaCoO_3$ as cathode materials for a doped $LaGaO_3$ ceramic fuel cell. *J. Electrochem. Soc.* **1996**, *143* (11), 3630−3636.

(28) Hu, S.; Zhang, L.; Cao, Z.; Yu, W.; Zhang, P.; Zhu, X.; Yang, W. Cathode activation process and CO_2 electroreduction mechanism on $LnFeO_{3-\delta}$ (Ln = La, Pr and Gd) perovskite cathodes. *J. Power Sources* **2021**, *485*, 229343.

(29) Yang, X. X.; Sun, K. N.; Ma, M. J.; Xu, C. M.; Ren, R. Z.; Qiao, J. S.; Wang, Z. H.; Zhen, S. Y.; Hou, R. J.; Sun, W. Achieving strong chemical adsorption ability for efficient carbon dioxide electrolysis. *Appl. Catal. B: Environ.* **2020**, *272*, 118968.

(30) Tian, Y. F.; Liu, Y.; Jia, L. C.; Naden, A.; Chen, J.; Chi, B.; Pu, J.; Irvine, J. T. S.; Li, J. A novel electrode with multifunction and regeneration for highly efficient and stable symmetrical solid oxide cell. *J. Power Sources* **2020**, *475*, 228620.

(31) Ebbesen, S. D.; Knibbe, R.; Mogensen, M. Co-Electrolysis of steam and carbon dioxide in solid oxide cells. *J. Electrochem. Soc.* **2012**, *159* (8), F482−F489.

(32) Ebbesen, S. D.; Sun, X. F.; Mogensen, M. B. Understanding the processes governing performance and durability of solid oxide electrolysis cells. *Faraday Discuss.* **2015**, *182*, 393−422.

(33) Carneiro, J.; Nikolla, E. Nanoengineering of solid oxide electrochemical cell technologies: An outlook. *Nano Res.* **2019**, *12* (9), 2081−2092.

(34) Cadi-Essadek, A.; Roldan, A.; Aparicio-Anglès, X.; de Leeuw, N. H. CO_2 and H_2 adsorption and reaction at Ni_n/YSZ(111) interfaces: A density functional theory study. *J. Phys. Chem. C* **2018**, *122* (34), 19463−19472.

(35) Chen, K.; Jiang, S. P. Review - Materials degradation of solid oxide electrolysis cells. *J. Electrochem. Soc.* **2016**, *163* (11), F3070−F3083.

(36) Yue, W.; Li, Y.; Zheng, Y.; Wu, T.; Zhao, C.; Zhao, J.; Geng, G.; Zhang, W.; Chen, J.; Zhu, J.; Yu, B. Enhancing coking resistance of Ni/YSZ electrodes: In situ characterization, mechanism research, and surface engineering. *Nano Energy* **2019**, *62*, 64−78.

(37) Zhang, X. M.; Song, Y. F.; Wang, G. X.; Bao, X. H. Co-electrolysis of CO_2 and H_2O in high-temperature solid oxide electrolysis cells: Recent advance in cathodes. *J. Energy Chem.* **2017**, *26* (5), 839−853.

(38) Mauvy, F.; Fouletier, J. Determination of thermodynamic and transport properties of non-stoichiometric oxides. In *Stoichiometry and materials science - When numbers matter*; Innocenti, A., Kamarulzaman, N., Eds.; IntechOpen: 2012.

(39) Tuller, H. L. 6 - Mixed conduction in nonstoichiometric oxides. In *Nonstoichiometric oxides?-*, Sørensen, O. T., Ed.; Academic Press: 1981; pp 271−335.

(40) Budiman, R. A.; Hong, H. J.; Hashimoto, S.; Nakamura, T.; Yamaji, K.; Yashiro, K.; Amezawa, K.; Kawada, T. Electronic conduction mechanism and defect chemical model of $LaNi_{0.4}Fe_{0.6}O_{3-\delta}$. *Solid State Ion.* **2017**, *310*, 148−153.

(41) Samira, S.; Camayang, J. C. A.; Patel, K.; Gu, X.-K.; Nikolla, E. Modulating catalytic properties of targeted metal cationic centers in nonstochiometric mixed metal oxides for electrochemical oxygen reduction. *ACS Energy Lett.* **2021**, *6* (3), 1065−1072.

(42) Linstrom, P. J.; Mallard, W. G. NIST Chemistry WebBook, NIST standard reference database Number 69. DOI: 10.18434/T4D303 (accessed May 27, 2022).

(43) Ren, B.; Croiset, E.; Ricardez-Sandoval, L. A theoretical study on CO_2 electrolysis through synergistic manipulation of Ni/Mn doping and oxygen vacancies in $La(Sr)FeO_3$. *J. Catal.* **2020**, *383*, 273−282.

(44) Kozokaro, V. F.; Addo, P. K.; Ansari, H. M.; Birss, V. I.; Toroker, M. C. Optimal oxygen vacancy concentration for CO_2 reduction in LSFCr perovskite: A combined density functional theory and thermogravimetric analysis Measurement Study. *J. Phys. Chem. C* **2020**, *124* (50), 27453−27466.

(45) Gu, X.-K.; Carneiro, J. S. A.; Nikolla, E. First-Principles study of high temperature CO_2 electrolysis on transition metal electrocatalysts. *Ind. Eng. Chem. Res.* **2017**, *56* (21), 6155−6163.

(46) Carneiro, J.; Gu, X.-K.; Tezel, E.; Nikolla, E. Electrochemical reduction of CO_2 on metal-based cathode electrocatalysts of solid oxide electrolysis cells. *Ind. Eng. Chem. Res.* **2020**, *59* (36), 15884−15893.

(47) Jiang, Y. A.; Chen, F. L.; Xia, C. R. A review on cathode processes and materials for electro-reduction of carbon dioxide in solid oxide electrolysis cells. *J. Power Sources* **2021**, *493*, 229713.

(48) Yang, J.; Hu, S.; Fang, Y.; Hoang, S.; Li, L.; Yang, W.; Liang, Z.; Wu, J.; Hu, J.; Xiao, W.; Pan, C.; Luo, Z.; Ding, J.; Zhang, L.; Guo, Y. Oxygen vacancy promoted O_2 activation over perovskite oxide for low-temperature CO oxidation. *ACS Catal.* **2019**, *9* (11), 9751−9763.

(49) Zhu, J.; Zhang, W.; Li, Y.; Yue, W.; Geng, G.; Yu, B. Enhancing CO_2 catalytic activation and direct electroreduction on in-situ exsolved Fe/MnO_x nanoparticles from $(Pr,Ba)_2Mn_{2-y}Fe_yO_{5+\delta}$ layered perovskites for SOEC cathodes. *Appl. Catal. B: Environ* **2020**, *268*, 118389.

(50) Curnan, M. T.; Kitchin, J. R. Effects of concentration, crystal structure, magnetism, and electronic structure method on first-principles oxygen vacancy formation energy trends in perovskites. *J. Phys. Chem. C* **2014**, *118* (49), 28776−28790.

(51) Ishihara, T.; Wang, S.; Wu, K. T. Highly active oxide cathode of $La(Sr)Fe(Mn)O_3$ for intermediate temperature CO_2 and CO_2-H_2O co-electrolysis using LSGM electrolyte. *Solid State Ion.* **2017**, *299*, 60−63.

(52) Tezel, E.; Guo, D.; Whitten, A.; Yarema, G.; Freire, M.; Denecke, R.; McEwen, J.-S.; Nikolla, E. Elucidating the role of B-site cations toward CO_2 reduction in perovskite-based solid oxide electrolysis cells. *J. Electrochem. Soc.* **2022**, *169* (3), 034532.

(53) Hu, S.; Zhang, L.; Liu, H.; Cao, Z.; Yu, W.; Zhu, X.; Yang, W. Alkaline-earth elements (Ca, Sr and Ba) doped $LaFeO_{3-\delta}$ cathodes for CO_2 electroreduction. *J. Power Sources* **2019**, *443*, 227268.

(54) Yang, Y.; Li, Y.; Jiang, Y.; Zheng, M.; Hong, T.; Wu, X.; Xia, C. The electrochemical performance and CO_2 reduction mechanism on strontium doped lanthanum ferrite fuel electrode in solid oxide electrolysis cell. *Electrochim. Acta* **2018**, *284*, 159−167.

(55) Wang, S.; Jiang, H. G.; Gu, Y. H.; Yin, B.; Chen, S. N.; Shen, M. Y.; Zheng, Y. F.; Ge, L.; Chen, H.; Guo, L. C. Mo-doped $La_{0.6}Sr_{0.4}FeO_{3-\delta}$ as an efficient fuel electrode for direct electrolysis of CO_2 in solid oxide electrolysis cells. *Electrochim. Acta* **2020**, *337*, 135794.

(56) Zhou, Y. J.; Zhou, Z. W.; Song, Y. F.; Zhang, X. M.; Guan, F.; Lv, H. F.; Liu, Q. X.; Miao, S.; Wang, G. X.; Bao, X. H. Enhancing CO_2 electrolysis performance with vanadium-doped perovskite cathode in solid oxide electrolysis cell. *Nano Energy* **2018**, *50*, 43−51.

(57) Peng, X.; Tian, Y.; Liu, Y.; Wang, W.; Jia, L.; Pu, J.; Chi, B.; Li, J. An efficient symmetrical solid oxide electrolysis cell with LSFM-based electrodes for direct electrolysis of pure CO_2. *J. CO_2 Util.* **2020**, *36*, 18−24.

(58) Liu, L. M.; Zhou, X. L.; Wang, Y.; Li, S.; Yin, R.; Guo, P.; Zhao, J. G.; Zhao, X. H.; Li, B. Composite ceramic cathode $La_{0.9}Ca_{0.1}Fe_{0.9}Nb_{0.1}O_{3\text{-delta}}/Sc_{0.2}Zr_{0.8}O_{2-\delta}$ towards efficient carbon dioxide electrolysis in zirconia-based high temperature electrolyser. *Int. J. Hydrogen Energy* **2017**, *42* (22), 14905−14915.

(59) Liu, L. M.; Zhou, X. L.; Wang, Y.; Li, S.; Yin, R.; Ji, X. Y.; Zhao, X. H.; Li, B. Study of high active and redox-stable $La_{0.9}Ca_{0.1}Fe_{0.9}Nb_{0.1}O_{3-\delta}/Sm_{0.1}Ce_{0.9}O_{2-\delta}$ composite ceramic electrode for solid oxide reversible cells. *Electrochim. Acta* **2017**, *236*, 371−377.

(60) Hou, Y. T.; Wang, L. J.; Bian, L. Z.; Wang, Y. D.; Chou, K. C.; Kumar, R. V. High-performance $La_{0.3}Sr_{0.7}Fe_{0.9}Ti_{0.1}O_{3-\delta}$ as fuel electrode for directly electrolyzing CO_2 in solid oxide electrolysis cells. *Electrochim. Acta* **2020**, *342*, 136026.

(61) Tian, Y.; Zheng, H.; Zhang, L.; Chi, B.; Pu, J.; Li, J. Direct electrolysis of CO_2 in symmetrical solid oxide electrolysis cell based on $La_{0.6}Sr_{0.4}Fe_{0.8}Ni_{0.2}O_{3-\delta}$ electrode. *J. Electrochem. Soc.* **2018**, *165* (2), F17−F23.

(62) Liu, S.; Liu, Q.; Luo, J.-L. The excellence of $La(Sr)Fe(Ni)O_3$ as an active and efficient cathode for direct CO_2 electrochemical reduction at elevated temperatures. *J. Mater. Chem. A* **2017**, *5* (6), 2673−2680.

(63) Addo, P. K.; Molero-Sanchez, B.; Chen, M.; Paulson, S.; Birss, V. CO/CO_2 study of high performance $La_{0.3}Sr_{0.7}Fe_{0.7}Cr_{0.3}O_{3-\delta}$ reversible SOFC electrodes. *Fuel Cells* **2015**, *15* (5), 689−696.

(64) Cao, Z. Q.; Wei, B.; Miao, J. P.; Wang, Z. H.; Lu, Z.; Li, W. Y.; Zhang, Y. H.; Huang, X. Q.; Zhu, X. B.; Feng, Q.; Sui, Y. Efficient electrolysis of CO_2 in symmetrical solid oxide electrolysis cell with

highly active $La_{0.3}Sr_{0.7}Fe_{0.7}Ti_{0.3}O_3$ electrode material. *Electrochem. Commun.* **2016**, *69*, 80−83.

(65) Cao, Z. Q.; Wang, Z. H.; Li, F. J.; Maliutina, K.; Wu, Q. X.; He, C. X.; Lv, Z.; Fan, L. D. Insight into high electrochemical activity of reduced $La_{0.3}Sr_{0.7}Fe_{0.7}Ti_{0.3}O_3$ electrode for high temperature CO_2 electrolysis. *Electrochim. Acta* **2020**, *332*, 135464.

(66) Lu, J. H.; Li, S. S.; Tao, S. W.; Zhang, T.; Xie, K. Efficient CO_2 electrolysis with scandium doped titanate cathode. *Int. J. Hydrogen Energy* **2017**, *42* (12), 8197−8206.

(67) Cui, C. S.; Wang, Y.; Tong, Y. C.; Zhan, Z. L.; Chen, C. S.; Wang, S. W. Direct CO_2 electrolysis on symmetric $La_{0.8}Sr_{0.2}Cr_{0.5}Fe_{0.5}O_{3-\delta}$-$Zr_{0.84}Y_{0.16}O_{2-\delta}$ electrode-supported solid oxide electrolysis cells. *J. Electrochem. Soc.* **2021**, *168* (2), 024508.

(68) Ruan, C.; Xie, K. A redox-stable chromate cathode decorated with in situ grown nickel nanocatalyst for efficient carbon dioxide electrolysis. *Catal. Sci. Technol.* **2015**, *5* (3), 1929−1940.

(69) Xu, S. S.; Li, S. S.; Yao, W. T.; Dong, D. H.; Xie, K. Direct electrolysis of CO_2 using an oxygen-ion conducting solid oxide electrolyzer based on $La_{0.75}Sr_{0.25}Cr_{0.5}Mn_{0.5}O_{3-\delta}$ electrode. *J. Power Sources* **2013**, *230*, 115−121.

(70) Lee, S.; Kim, M.; Lee, K. T.; Irvine, J. T. S.; Shin, T. H. Enhancing electrochemical CO_2 reduction using Ce(Mn,Fe)O_2 with La(Sr)Cr(Mn)O_3 cathode for high-temperature solid oxide electrolysis cells. *Adv. Energy Mater.* **2021**, *11*, 2100339.

(71) Ye, L. T.; Hu, X. L.; Wang, X.; Chen, F. L.; Tang, D.; Dong, D. H.; Xie, K. Enhanced CO_2 electrolysis with a $SrTiO_3$ cathode through a dual doping strategy. *J. Mater. Chem. A* **2019**, *7* (6), 2764−2772.

(72) Ye, L. T.; Zhang, M. Y.; Huang, P.; Guo, G. C.; Hong, M. C.; Li, C. S.; Irvine, J. T. S.; Xie, K. Enhancing CO_2 electrolysis through synergistic control of non-stoichiometry and doping to tune cathode surface structures. *Nat. Commun.* **2017**, *8*, 14785.

(73) Qi, W.; Gan, Y.; Yin, D.; Li, Z.; Wu, G.; Xie, K.; Wu, Y. Remarkable chemical adsorption of manganese-doped titanate for direct carbon dioxide electrolysis. *J. Mater. Chem. A* **2014**, *2* (19), 6904−6915.

(74) Yang, L. M.; Xie, K.; Wu, L.; Qin, Q. Q.; Zhang, J.; Zhang, Y.; Xie, T.; Wu, Y. C. A composite cathode based on scandium doped titanate with enhanced electrocatalytic activity towards direct carbon dioxide electrolysis. *Phys. Chem. Chem. Phys.* **2014**, *16* (39), 21417−21428.

(75) Kaur, G.; Kulkarni, A. P.; Giddey, S. CO_2 reduction in a solid oxide electrolysis cell with a ceramic composite cathode: Effect of load and thermal cycling. *Int. J. Hydrogen Energy* **2018**, *43* (48), 21769−21776.

(76) Ji, Q.; Bi, L.; Zhang, J.; Cao, H.; Zhao, X. S. The role of oxygen vacancies of ABO_3 perovskite oxides in the oxygen reduction reaction. *Energy Environ. Sci.* **2020**, *13*, 1408−1428.

(77) Chen, Y.; Téllez, H.; Burriel, M.; Yang, F.; Tsvetkov, N.; Cai, Z.; McComb, D. W.; Kilner, J. A.; Yildiz, B. Segregated chemistry and structure on (001) and (100) surfaces of $(La_{1-x}Sr_x)_2CoO_4$ override the crystal anisotropy in oxygen exchange kinetics. *Chem. Mater.* **2015**, *27* (15), 5436−5450.

(78) Lee, D.; Lee, Y.-L.; Grimaud, A.; Hong, W. T.; Biegalski, M. D.; Morgan, D.; Shao-Horn, Y. Strontium influence on the oxygen electrocatalysis of $La_{2-x}Sr_xNiO_{4\pm\delta}$ ($0.0 \le x_{Sr} \le 1.0$) thin films. *J. Mater. Chem. A* **2014**, *2* (18), 6480−6487.

(79) Baiyee, Z. M.; Chen, C.; Ciucci, F. A DFT+U study of A-site and B-site substitution in $BaFeO_{3-\delta}$. *Phys. Chem. Chem. Phys.* **2015**, *17* (36), 23511−23520.

(80) Ma, Z.; Zhou, J.; Li, Y.; Liu, C.; Pu, J.; Chen, X. Developments in CO_2 electrolysis of solid oxide electrolysis cell with different cathodes. *Fuel Cells* **2020**, *20* (6), 650−660.

(81) Mizusaki, J.; Sasamoto, T.; Cannon, W. R.; Bowen, H. K. Electronic conductivity, seebeck coefficient, and defect structure of $La_{1-x}Sr_xFeO_3$ (x = 0.1, 0.25). *J. Am. Ceram. Soc.* **1983**, *66* (4), 247−252.

(82) Aguadero, A.; Fawcett, L.; Taub, S.; Woolley, R.; Wu, K.-T.; Xu, N.; Kilner, J. A.; Skinner, S. J. Materials development for intermediate-temperature solid oxide electrochemical devices. *J. Mater. Sci.* **2012**, *47* (9), 3925−3948.

(83) Opitz, A. K.; Nenning, A.; Rameshan, C.; Kubicek, M.; Götsch, T.; Blume, R.; Hävecker, M.; Knop-Gericke, A.; Rupprechter, G.; Klötzer, B.; Fleig, J. Surface chemistry of perovskite-type electrodes during high temperature CO_2 electrolysis investigated by operando photoelectron spectroscopy. *ACS Appl. Mater. Interfaces* **2017**, *9* (41), 35847−35860.

(84) Ren, B. H.; Croiset, E.; Ricardez-Sandoval, L. A theoretical study on CO_2 electrolysis through synergistic manipulation of Ni/Mn doping and oxygen vacancies in La(Sr)FeO_3. *J. Catal.* **2020**, *383*, 273−282.

(85) Wang, X.; Miyazaki, T.; Yashiro, K.; Hashimoto, S.; Kawada, T. The origin of instability of lanthanum strontium cobalt ferrite (La−Sr−Co−Fe−O; LSCF) under oxygen potential gradient. *ECS Trans.* **2017**, *75* (28), 1−9.

(86) Ling, Y.; Wang, F.; Budiman, R. A.; Nakamura, T.; Amezawa, K. Oxygen nonstoichiometry, the defect equilibrium model and thermodynamic quantities of the Ruddlesden−Popper oxide $Sr_3Fe_2O_{7-\delta}$. *Phys. Chem. Chem. Phys.* **2015**, *17* (11), 7489−7497.

(87) Ishihara, T.; Wu, K. T.; Wang, S. (Invited) High temperature CO_2 electrolysis on La(Sr)Fe(Mn)O_3 oxide cathode by using $LaGaO_3$ based electrolyte. *ECS Trans.* **2015**, *66* (2), 197−205.

(88) Li, Y.; Chen, X.; Yang, Y.; Jiang, Y.; Xia, C. Mixed-conductor $Sr_2Fe_{1.5}Mo_{0.5}O_{6-\delta}$ as robust fuel electrode for pure CO_2 reduction in solid oxide electrolysis cell. *ACS Sustain. Chem. Eng.* **2017**, *5* (12), 11403−11412.

(89) Das, A.; Xhafa, E.; Nikolla, E. Electro- and thermal-catalysis by layered, first series Ruddlesden-Popper oxides. *Catal. Today* **2016**, *277*, 214−226.

(90) Huan, D.; Zhang, L.; Zhang, S.; Shi, N.; Li, X.; Zhu, K.; Xia, C.; Peng, R.; Lu, Y. Ruddlesden−Popper oxide $SrEu_2Fe_2O_7$ as a promising symmetrical electrode for pure CO_2 electrolysis. *J. Mater. Chem. A* **2021**, *9* (5), 2706−2713.

(91) Lv, H.; Liu, T.; Zhang, X.; Song, Y.; Matsumoto, H.; Ta, N.; Zeng, C.; Wang, G.; Bao, X. Atomic-Scale insight into exsolution of CoFe alloy nanoparticles in $La_{0.4}Sr_{0.6}Co_{0.2}Fe_{0.7}Mo_{0.1}O_{3-\delta}$ with efficient CO_2 electrolysis. *Angew. Chem. Int. Ed.* **2020**, *59* (37), 15968−15973.

(92) Tian, Y.; Liu, Y.; Naden, A.; Jia, L.; Xu, M.; Cui, W.; Chi, B.; Pu, J.; Irvine, J. T. S.; Li, J. Boosting CO_2 electrolysis performance via calcium-oxide-looping combined with in situ exsolved Ni−Fe nanoparticles in a symmetrical solid oxide electrolysis cell. *J. Mater. Chem. A* **2020**, *8* (30), 14895−14899.

(93) Liu, C. Y.; Li, S. T.; Gao, J. Q.; Bian, L. Z.; Hou, Y. T.; Wang, L. J.; Peng, J.; Bao, J. X.; Song, X. W.; An, S. L. Enhancing CO_2 catalytic adsorption on an Fe nanoparticle-decorated $LaSrFeO_{4+\delta}$ cathode for CO_2 electrolysis. *ACS Appl. Mater. Inter* **2021**, *13* (7), 8229−8238.

(94) Liu, S.; Liu, Q.; Luo, J.-L. Highly stable and efficient catalyst with in situ exsolved Fe−Ni alloy nanospheres socketed on an oxygen deficient perovskite for direct CO_2 electrolysis. *ACS Catal.* **2016**, *6* (9), 6219−6228.

(95) Li, Y. H.; Hu, B. B.; Xia, C. R.; Xu, W. Q.; Lemmon, J. P.; Chen, F. L. A novel fuel electrode enabling direct CO_2 electrolysis with excellent and stable cell performance. *J. Mater. Chem. A* **2017**, *5* (39), 20833−20842.

(96) Park, S.; Kim, Y.; Noh, Y.; Kim, T.; Han, H.; Yoon, W.; Choi, J.; Yi, S. H.; Leec, W. J.; Kim, W. B. A sulfur-tolerant cathode catalyst fabricated with in situ exsolved CoNi alloy nanoparticles anchored on a Ruddlesden-Popper support for CO_2 electrolysis. *J. Mater. Chem. A* **2020**, *8* (1), 138−148.

(97) Yang, X. X.; Sun, W.; Ma, M. J.; Xu, C. M.; Ren, R. Z.; Qiao, J. S.; Wang, Z. H.; Li, Z. S.; Zhen, S. Y.; Sun, K. N. Achieving highly efficient carbon dioxide electrolysis by in situ construction of the heterostructure. *ACS Appl. Mater. Interfaces* **2021**, *13* (17), 20060−20069.

(98) Li, H.; Sun, G.; Xie, K.; Qi, W.; Qin, Q.; Wei, H.; Chen, S.; Wang, Y.; Zhang, Y.; Wu, Y. Chromate cathode decorated with in-situ

growth of copper nanocatalyst for high temperature carbon dioxide electrolysis. *Int. J. Hydrogen Energy* **2014**, *39* (36), 20888−20897.

(99) Zhang, J.; Xie, K.; Zhang, Y.; Yang, L.; Wu, G.; Qin, Q.; Li, Y.; Wu, Y. Composite titanate cathode decorated with heterogeneous electrocatalytic sites towards efficient carbon dioxide electrolysis. *RSC Adv.* **2014**, *4* (43), 22697−22709.

(100) Li, Y. X.; Xie, K.; Chen, S. G.; Li, H. X.; Zhang, Y.; Wu, Y. C. Efficient carbon dioxide electrolysis based on perovskite cathode enhanced with nickel nanocatalyst. *Electrochim. Acta* **2015**, *153*, 325−333.

(101) Choi, J.; Park, S.; Han, H.; Kim, M.; Park, M.; Han, J.; Kim, W. B. Highly efficient CO_2 electrolysis to CO on Ruddlesden-Popper perovskite oxide with in situ exsolved Fe nanoparticles dagger. *J. Mater. Chem. A* **2021**, *9*, 8740−8748.

(102) Park, S.; Kim, Y.; Han, H.; Chung, Y. S.; Yoon, W.; Choi, J.; Kim, W. B. In situ exsolved Co nanoparticles on Ruddlesden-Popper material as highly active catalyst for CO_2 electrolysis to CO. *Appl. Catal. B:Environ* **2019**, *248*, 147−156.

(103) Sun, Y. F.; Zhang, Y. Q.; Chen, J.; Li, J. H.; Zhu, Y. T.; Zeng, Y. M.; Amirkhiz, B. S.; Li, J.; Hua, B.; Luo, J. L. New opportunity for in situ exsolution of metallic nanoparticles on perovskite parent. *Nano Lett.* **2016**, *16* (8), 5303−5309.

(104) Gan, L. Z.; Ye, L. T.; Tao, S. W.; Xie, K. Titanate cathodes with enhanced electrical properties achieved via growing surface Ni particles toward efficient carbon dioxide electrolysis. *Phys. Chem. Chem. Phys.* **2016**, *18* (4), 3137−3143.

(105) Gan, J. J.; Hou, N. J.; Yao, T. T.; Fan, L. J.; Gan, T.; Huang, Z. Y.; Zhao, Y. C.; Li, Y. D. A high performing perovskite cathode with in situ exsolved Co nanoparticles for H_2O and CO_2 solid oxide electrolysis cell. *Catal. Today* **2021**, *364*, 89−96.

(106) Lv, H.; Lin, L.; Zhang, X.; Gao, D.; Song, Y.; Zhou, Y.; Liu, Q.; Wang, G.; Bao, X. In situ exsolved $FeNi_3$ nanoparticles on nickel doped $Sr_2Fe_{1.5}Mo_{0.5}O_{6-\delta}$ perovskite for efficient electrochemical CO_2 reduction reaction. *J. Mater. Chem. A* **2019**, 7 (19), 11967−11975.

(107) Thommy, L.; Joubert, O.; Hamon, J.; Caldes, M.-T. Impregnation versus exsolution: Using metal catalysts to improve electrocatalytic properties of LSCM-based anodes operating at 600 °C. *Int. J. Hydrogen Energy* **2016**, *41* (32), 14207−14216.

(108) Ulumuddin, N.; Che, F.; Yang, J.-I.; Ha, S.; McEwen, J.-S. Elucidating the influence of electric fields toward CO_2 activation on YSZ (111). *Catalysts* **2021**, *11* (2), 271.

(109) Kotiuga, M.; Zhang, Z.; Li, J.; Rodolakis, F.; Zhou, H.; Sutarto, R.; He, F.; Wang, Q.; Sun, Y.; Wang, Y.; Aghamiri, N. A.; Hancock, S. B.; Rokhinson, L. P.; Landau, D. P.; Abate, Y.; Freeland, J. W.; Comin, R.; Ramanathan, S.; Rabe, K. M. Carrier localization in perovskite nickelates from oxygen vacancies. *Proc. Natl. Acad. Sci. U.S.A.* **2019**, *116* (44), 21992.

(110) Montoya, J. H.; Doyle, A. D.; Norskov, J. K.; Vojvodic, A. Trends in adsorption of electrocatalytic water splitting intermediates on cubic ABO_3 oxides. *Phys. Chem. Chem. Phys.* **2018**, *20* (5), 3813−3818.

(111) Yoo, J. S.; Rong, X.; Liu, Y.; Kolpak, A. M. Role of lattice oxygen participation in understanding trends in the oxygen evolution reaction on perovskites. *ACS Catal.* **2018**, *8* (5), 4628−4636.

(112) Samira, S.; Gu, X.-K.; Nikolla, E. Design strategies for efficient nonstoichiometric mixed metal oxide electrocatalysts: Correlating measurable oxide properties to electrocatalytic performance. *ACS Catal.* **2019**, *9* (11), 10575−10586.

(113) Lu, Y.; Ma, A.; Yu, Y.; Tan, R.; Liu, C.; Zhang, P.; Liu, D.; Gui, J. Engineering oxygen vacancies into $LaCoO_3$ perovskite for efficient electrocatalytic oxygen evolution. *ACS Sustain. Chem. Eng.* **2019**, *7* (3), 2906−2910.

(114) Mastrikov, Y. A.; Merkle, R.; Kotomin, E. A.; Kuklja, M. M.; Maier, J. Formation and migration of oxygen vacancies in $La_{1-x}Sr_xCo_{1-y}Fe_yO_{3-\delta}$ perovskites: insight from ab initio calculations and comparison with $Ba_{1-x}Sr_xCo_{1-y}Fe_yO_{3-\delta}$. *Phys. Chem. Chem. Phys.* **2013**, *15* (3), 911−918.

(115) Ding, S.; Li, M.; Pang, W.; Hua, B.; Duan, N.; Zhang, Y.-Q.; Zhang, S.-N.; Jin, Z.; Luo, J.-L. A-site deficient perovskite with nano-socketed Ni-Fe alloy particles as highly active and durable catalyst for high-temperature CO_2 electrolysis. *Electrochim. Acta* **2020**, *335*, 135683.

(116) Lv, H.; Liu, T.; Zhang, X.; Yuefeng, S.; Matsumoto, H.; Ta, N.; Zeng, C.; Wang, G.; Bao, X. Atomic-Scale Insight into Exsolution of CoFe Alloy Nanoparticles in $La_{0.4}Sr_{0.6}Co_{0.2}Fe_{0.7}Mo_{0.1}O_{3-\delta}$ with Efficient CO_2 Electrolysis. *Angew. Chem.* **2020**, *59*, 15968.

(117) Yang, X.; Sun, W.; Ma, M.; Xu, C.; Ren, R.; Qiao, J.; Wang, Z.; Li, Z.; Zhen, S.; Sun, K. Achieving Highly Efficient Carbon Dioxide Electrolysis by In Situ Construction of the Heterostructure. *ACS Appl. Mater. Interfaces* **2021**, *13* (17), 20060−20069.

(118) Ye, L.; Zhang, M.; Huang, P.; Guo, G.; Hong, M.; Li, C.; Irvine, J. T. S.; Xie, K. Enhancing CO_2 electrolysis through synergistic control of non-stoichiometry and doping to tune cathode surface structures. *Nat. Commun.* **2017**, *8* (1), 14785.

(119) Nolan, M.; Parker, S. C.; Watson, G. W. The electronic structure of oxygen vacancy defects at the low index surfaces of ceria. *Surf. Sci.* **2005**, *595* (1), 223−232.

(120) Carneiro, J. S. A.; Brocca, R. A.; Lucena, M. L. R. S.; Nikolla, E. Optimizing cathode materials for intermediate-temperature solid oxide fuel cells (SOFCs): Oxygen reduction on nanostructured lanthanum nickelate oxides. *Appl. Catal. B: Environ.* **2017**, *200*, 106−113.

(121) Green, R. D.; Liu, C.-C.; Adler, S. B. Carbon dioxide reduction on gadolinia-doped ceria cathodes. *Solid State Ion.* **2008**, *179* (17), 647−660.

(122) Jiang, Y.; Chen, F.; Xia, C. A review on cathode processes and materials for electro-reduction of carbon dioxide in solid oxide electrolysis cells. *J. Power Sources* **2021**, *493*, 229713.

(123) Pomfret, M. B.; Owrutsky, J. C.; Walker, R. A. In situ studies of fuel oxidation in solid oxide fuel cells. *Anal. Chem.* **2007**, *79* (6), 2367−2372.

(124) Pomfret, M. B.; Marda, J.; Jackson, G. S.; Eichhorn, B. W.; Dean, A. M.; Walker, R. A. Hydrocarbon fuels in solid oxide fuel cells: In situ Raman studies of graphite formation and oxidation. *J. Phys. Chem. C* **2008**, *112* (13), 5232−5240.

(125) Traulsen, M. L.; de Carvalho, H. W. P.; Zielke, P.; Grunwaldt, J. D. The effect of electrical polarization on electronic structure in LSM electrodes: An operando XAS, RIXS and XES study. *J. Electrochem. Soc.* **2017**, *164* (10), F3064−F3072.

(126) Zhang, C.; Grass, M. E.; Yu, Y.; Gaskell, K. J.; DeCaluwe, S. C.; Chang, R.; Jackson, G. S.; Hussain, Z.; Bluhm, H.; Eichhorn, B. W.; Liu, Z. Multielement activity mapping and potential mapping in solid oxide electrochemical cells through the use of operando XPS. *ACS Catal.* **2012**, *2* (11), 2297−2304.

(127) El Gabaly, F.; Grass, M.; McDaniel, A. H.; Farrow, R. L.; Linne, M. A.; Hussain, Z.; Bluhm, H.; Liu, Z.; McCarty, K. F. Measuring individual overpotentials in an operating solid-oxide electrochemical cell. *Phys. Chem. Chem. Phys.* **2010**, *12* (38), 12138−12145.

(128) Xu, Z.; Rossmeisl, J.; Kitchin, J. R. A linear response DFT+U study of trends in the oxygen evolution activity of transition metal rutile dioxides. *J. Phys. Chem. C* **2015**, *119* (9), 4827−4833.

(129) Kulik, H. J. Perspective: Treating electron over-delocalization with the DFT+U method. *J. Chem. Phys.* **2015**, *142* (24), 240901.

(130) Qiao, B.; Wang, A.; Yang, X.; Allard, L. F.; Jiang, Z.; Cui, Y.; Liu, J.; Li, J.; Zhang, T. Single-atom catalysis of CO oxidation using Pt_1/FeO_x. *Nat. Chem.* **2011**, *3* (8), 634−641.

(131) Hensley, A. J. R.; Wang, Y.; McEwen, J.-S. The partial reduction of clean and doped α-Fe_2O_3(0001) from first principles. *Appl. Catal. A: Gen.* **2019**, *582*, 116989.

(132) Sun, J.; Ruzsinszky, A.; Perdew, J. P. Strongly constrained and appropriately normed semilocal density functional. *Phys. Rev. Lett.* **2015**, *115* (3), 036402.

(133) Krukau, A. V.; Vydrov, O. A.; Izmaylov, A. F.; Scuseria, G. E. Influence of the exchange screening parameter on the performance of screened hybrid functionals. *J. Phys. Chem. C* **2006**, *125* (22), 224106.

(134) Dovesi, R.; Erba, A.; Orlando, R.; Zicovich-Wilson, C. M.; Civalleri, B.; Maschio, L.; Rérat, M.; Casassa, S.; Baima, J.; Salustro,

S.; Kirtman, B. Quantum-mechanical condensed matter simulations with CRYSTAL. *WIRES Comput. Mol. Sci.* **2018**, *8* (4), No. e1360.

(135) Clark, M. L.; Ge, A.; Videla, P. E.; Rudshteyn, B.; Miller, C. J.; Song, J.; Batista, V. S.; Lian, T.; Kubiak, C. P. CO_2 reduction catalysts on gold electrode surfaces influenced by large electric fields. *J. Am. Chem. Soc.* **2018**, *140* (50), 17643−17655.

(136) Liang, T.; Cheng, Y.-T.; Nie, X.; Luo, W.; Asthagiri, A.; Janik, M. J.; Andrews, E.; Flake, J.; Sinnott, S. B. Molecular dynamics simulations of CO_2 reduction on Cu (111) and Cu/ZnO (1010) using charge optimized many body potentials. *Catal. Commun.* **2014**, *52*, 84−87.

(137) Cheng, T.; Xiao, H.; Goddard, W. A. Full atomistic reaction mechanism with kinetics for CO reduction on Cu (100) from ab initio molecular dynamics free-energy calculations at 298 K. *Proc. Natl. Acad. Sci. U.S.A.* **2017**, *114* (8), 1795−1800.